

Disk-Jet Coupling in Black Hole Accretion Systems II: Force-Free Electrodynamical Models

Jonathan C. McKinney¹ * and Ramesh Narayan^{1*}

¹*Institute for Theory and Computation, Center for Astrophysics, Harvard University, 60 Garden St., Cambridge, MA, 02138*

Accepted 2006 October 19. Received 2006 September 17; in original form 2006 July 25

ABSTRACT

In paper I, we showed that time-dependent general relativistic magnetohydrodynamic (GRMHD) numerical models of accretion disks, although being highly turbulent, have surprisingly simple electromagnetic properties. In particular, the toroidal current density in the disk takes the form $dI_\phi/dr \propto r^{-5/4}$. Guided by this simplicity, we use a time-dependent general relativistic force-free electrodynamics (GRFFE) code to study an idealized problem in which the accretion disk is replaced by an infinitely thin rotating equatorial current sheet. We consider both an $r^{-5/4}$ current profile and an r^{-1} profile, the latter corresponding to the paraboloidal model of Blandford & Znajek (1977). The force-free magnetosphere we obtain with the $r^{-5/4}$ current sheet matches remarkably well to the Poynting-dominated jet seen in GRMHD numerical models. By comparing to the non-rotating force-free model studied in paper I, rotation is seen to lead to mild decollimation of the jet suggesting that hoop-stress forces nearly cancel centrifugal forces. In order to study the process that generates the corona and disk wind and destroys the ordered field in the corona in GRMHD numerical models, the force-free field with the $r^{-5/4}$ current distribution is embedded in an accretion disk and followed in a GRMHD simulation. Field at high latitudes is continuously transported to larger radii leaving a corona with only disordered field, while in the equator the turbulent field is accreted. Reconnection and magnetic stresses contribute to a magnetized, thermal wind without the aid of an ordered field threading the disk.

Key words: accretion disks, black hole physics, galaxies: jets, gamma rays: bursts, X-rays : bursts

1 INTRODUCTION

Accretion disks around black holes have been recently studied using general relativistic magnetohydrodynamic (GRMHD) simulations that have been used to determine the structure of the disk, corona, wind, and Poynting-dominated jet (De Villiers, Hawley, & Krolik 2003; McKinney & Gammie 2004). This paper continues a study of the coupling between these components of the accretion flow.

The simulated accretion flows develop vigorous non-linear turbulence driven by the magneto-rotational instability (Balbus & Hawley 1991, 1998). One might suspect that all fluid and electromagnetic quantities in the disk would therefore be chaotic. However, as we showed in McKinney & Narayan (2006), the vertically integrated toroidal current exhibits a smooth and simple behavior

(McKinney & Narayan 2006). Specifically, the toroidal current I_ϕ enclosed inside radius r closely follows a power-law profile,

$$\frac{dI_\phi}{dr} \propto \frac{1}{r^{2-\nu}}, \quad (1)$$

with $\nu = 3/4$. This scaling is found to hold in a time-averaged sense but also at each instant of time. It is also independent of the black hole spin or the initial conditions used for the simulation. McKinney & Narayan (2006) argued that the presence of the simple current distribution is the reason why GRMHD models have simple, nearly steady, collimated, magnetically-dominated polar regions which are qualitatively similar in structure to the force-free jet in the Blandford-Znajek (1977, BZ) model (McKinney & Gammie 2004; Hawley & Krolik 2006; McKinney 2006c).

The fact that the current distribution in GRMHD models is simple suggests that the accretion disk might, at some level of approximation, be idealised as a simple boundary condition in the equatorial plane. Motivated by

* E-mail: jmcinney@cfa.harvard.edu (JCM); narayan@cfa.harvard.edu (RN)

this possibility, we consider general relativistic force-free electrodynamical (GRFFE) models with equatorial boundary conditions derived from GRMHD numerical models of turbulent accretion disks. Treating the accretion disk (or stellar surface) as a boundary condition is a commonly used device to obtain a basic understanding of jets and winds (see, e.g. Michel 1973; Okamoto 1974, 1978; Blandford 1976; Blandford & Payne 1982; Lovelace et al. 1986; Heyvaerts & Norman 1989; Nitta et al. 1991; Li et al. 1992; Appl & Camenzind 1992, 1993; Beskin & Pariev 1993; Contopoulos 1994; Contopoulos & Lovelace 1994; Contopoulos 1995a,b). The GRFFE approximation of the magnetosphere of the accretion disk leads to simple tractable equations that can be solved analytically (or quasi-analytically) in certain regimes, such as for slowly rotating black holes (Blandford & Znajek 1977) or for special field geometries (Uzdensky 2004, 2005).

The most famous GRFFE model that treats the disk as a boundary condition is the Blandford-Znajek (BZ) model (Blandford & Znajek 1977), which involves a stationary disk with a fixed toroidal current density. BZ presented two solutions for slowly spinning black holes with an equatorial current sheet. The first solution corresponds to a split-monopole field which is centered on the black hole; this solution is a general relativistic extension of the force-free pulsar magnetosphere solution of Michel (1973) and has a power-law disk current of the form given in equation (1) with $\nu = 0$. The second solution corresponds to a paraboloidal field, as in Blandford (1976), and has $\nu = 1$.

While the monopole solution is not applicable to collimating jets, BZ's paraboloidal solution is a potentially interesting model of astrophysical jets. However, the paraboloidal solution is incomplete because BZ do not ensure force balance across the boundary between field lines threading the black hole and those threading the equatorial accretion disk. BZ identified this interface between the black hole and accretion disk as the *transition region*. Their estimate of the energy output of the paraboloidal solution may be qualitatively incorrect since a significant amount of the energy comes from the transition region where the disk contacts the ergosphere. Since the work of Blandford & Znajek (1977), MacDonald (1984); Ghosh & Abramowicz (1997) considered better-motivated force-free solutions in order to estimate the flux ratio of the hole and disk but did not account for the transition region between the black hole and disk. Meliani et al. (2006) recently developed some small-angle approximations for the polar jet for a Schwarzschild black hole, while Uzdensky (2005) studied closed field (no jet) geometries for a Kerr black hole.

The difficulty of finding solutions to the GRFFE and GRMHD equations of motion has spawned a significant interest in developing time-dependent codes to solve these equations of motion. Of relevance to this paper is that time-dependent force-free codes found that the monopolar BZ solution (Komissarov 2001, 2002a,b, 2004) and the split-monopole BZ solution (McKinney 2006a) are stable. More recently force-free and MHD (in the highly magnetized limit) codes have been used to successfully study the pulsar magnetosphere in the regime that all field lines cross the light cylinder (Komissarov 2006; McKinney 2006b; Bucciantini et al. 2006; Spitkovsky 2006).

Our first objective in this paper is to use a time-

dependent GRFFE code (McKinney 2006a) to evolve the black hole + equatorial current sheet system with disk rotation and an arbitrarily rapidly rotating black hole to self-consistently obtain the complete paraboloidal-type field solution.

McKinney & Narayan (2006) found that the current distribution and poloidal funnel field geometry in GRMHD simulations of accretion disks are not consistent with BZ's paraboloidal model with $\nu = 1$ or BZ's monopolar model with $\nu = 0$. Instead, the best fit to the current distribution and the poloidal funnel field geometry is obtained with $\nu = 3/4$. Despite the apparent similarity between the $\nu = 1$ and $\nu = 3/4$ solutions, they are qualitatively different. For example, the $\nu = 1$ solution has a logarithmic divergence as a function of radius for the enclosed toroidal current. On the other hand, the $\nu = 3/4$ solution has a finite enclosed toroidal current. Given the similarity between the GRMHD simulations and the $\nu = 3/4$ current distribution and resulting funnel field geometry, our second objective is to solve the time-dependent GRFFE equations of motion for this GRMHD-motivated model with $\nu = 3/4$.

In order to construct a force-free model that closely matches the GRMHD simulations, we require not only the current density in the equatorial sheet but also the angular frequency of the field lines at the equator. The simple force-free models we described in McKinney & Narayan (2006) had no rotation, but here we are interested in modeling the effects of rotation. For this purpose we use the results of GRMHD simulations to construct a reasonable model of the field rotation frequency for the entire radial range from the horizon out well into the disk. McKinney & Narayan (2006) found that the disk field angular frequency is Keplerian at large radii but makes a smoothly transition near the black hole to $\Omega_F/\Omega_H \sim 0.5$ for $a/M \gtrsim 0.4$ and $\Omega_F/\Omega_H \sim 1$ for $a/M \lesssim 0.4$, where Ω_H is the angular frequency of the hole. A GRFFE solution with this dependence for Ω_F and a current distribution of $\nu = 3/4$ would be the closest a GRFFE model could come to the GRMHD simulations without including the vertical structure of the disk or the matter itself. Also, with Ω_F in the transition region modelled accurately, the energy output of the disk and the black hole can be measured and compared. We study and compare the jet structure in the idealized GRFFE model with that found in GRMHD simulations of accretion disks (McKinney 2006c) and find remarkable agreement between the two.

Our final objective is to demonstrate how the $\nu = 3/4$ force-free solution changes as a result of the presence of matter and the magneto-rotational instability. We choose the $\nu = 3/4$ type stationary field geometry as the initial conditions and carry out a GRMHD simulation with an accretion disk superimposed onto the field. We find that the model develops a turbulent disordered disk, corona and wind, but the Poynting-dominated jet power output is unchanged relative to the GRFFE model.

Paper Outline

In section 2, we outline the numerical setup and the method used to obtain force-free solutions. In section 3, we study the $\nu = 1$ paraboloidal force-free solution. In section 4, we study the $\nu = 3/4$ force-free solution using GRMHD-motivated boundary conditions for the disk. In section 5, we discuss

a GRMHD numerical model that is initialized with an accretion disk embedded with the $\nu = 3/4$ force-free field. We follow the destruction of the force-free field associated with the corona in GRMHD models. In section 6, we discuss the limitations of our calculations. Finally, in section 7, we discuss the results and conclude.

Units and Notation

The units in this paper have $GM = c = 1$, which sets the scale of length ($r_g \equiv GM/c^2$) and time ($t_g \equiv GM/c^3$). The density scale is arbitrary, so values of the density are normalized by some fiducial field strength. In order to convert to a physical value of the density for a given mass accretion rate, one must use the field strength as a function of black hole spin and mass accretion rate as given by GRMHD models such as described in McKinney (2005a,b,c, 2006c). The horizon is located at $r = r_+ \equiv r_g(1 + \sqrt{1 - (a/M)^2})$. For a black hole with angular momentum $J = aGM/c$, a/M is the dimensionless Kerr parameter with $-1 \leq a/M \leq 1$.

The notation follows Misner et al. (1973) and the signature of the metric is $-+++$. Tensor components are given in a coordinate basis. The components of the tensors of interest are given by $g_{\mu\nu}$ for the metric, $F^{\mu\nu}$ for the Faraday tensor, $\star F^{\mu\nu}$ for the dual of the Faraday, and $T^{\mu\nu}$ for the stress-energy tensor. The determinant of the metric is given by $\sqrt{-g} \equiv \text{Det}(g_{\mu\nu})$. The field angular frequency is $\Omega_F \equiv F_{t\theta}/F_{r\phi} = F_{t\theta}/F_{\theta\phi}$. The magnetic field can be written as $B^i = \star F^{it}$. The poloidal magnetospheric structure is defined by the ϕ -component of the vector potential (A_ϕ). The current system is defined by the current density (\mathbf{J}) and the polar enclosed poloidal current ($B_\phi \equiv \star F_{\phi t}$). The electromagnetic luminosity is $L \equiv -2\pi \int_\theta d\theta T^{(EM)t}_t r^2 \sin\theta$. See Gammie et al. (2003a); McKinney & Gammie (2004); McKinney (2004, 2005b,c, 2006a) for details on this standard notation. Kerr-Schild coordinates are used to avoid spurious reflections off the inner-radial boundary (McKinney & Gammie 2002).

2 GRFFE MODEL WITH DISK MAGNETOSPHERE

We study time-dependent GRFFE numerical models under the assumption that the turbulent accretion disk is well-modelled by an equatorial current sheet that is treated as a rotating conductor. The GRFFE code described in McKinney (2006a) is used to evolve the axisymmetric force-free equations of motion in the Kerr metric in Kerr-Schild coordinates. This code has also been successfully used to study pulsar magnetospheres (McKinney 2006b) and the split-monopole problem (McKinney 2006a). The computational grid geometry is chosen to be the same as in McKinney (2006c) with an inner radius inside the horizon and an outer radius at $10^3 r_g$. This grid focuses the resolution toward the polar axes at large radii in order to resolve the collimating jet.

The resolution for all models is chosen to be 256×256 , and the solutions are well-converged compared to low resolution models except very close to the poles due to the coordinate singularity in spherical polar coordinates.

2.1 Obtaining a Stationary Solution in GRFFE

Steady state GRFFE numerical models with no discontinuities or surface currents above the disk surface are found by choosing boundary conditions determined by an analysis of the Grad-Shafranov equation (see, e.g., Bogovalov 1997; Beskin 1997). For solutions that pass through a light cylinder at some radius, one is required to fix the magnetic field component B^θ perpendicular to the disk and specify 2 other constraints at the disk, viz., $E_\phi \equiv F_{t\phi} = 0$, and $\Omega_F = \Omega_{\text{disk}}$, the disk angular velocity. Note that one cannot leave both B^θ and B^r unconstrained, as this allows arbitrary redistribution of the currents in the disk. Doing so gives too much freedom and the solution reverts to the split-monopole solution. No boundary condition is applied on the black hole.

For axisymmetric, stationary solutions, the frozen-in condition of ideal MHD implies that the field line velocity v^i is completely determined by the field B^i and field rotation frequency Ω_F (see equation 46 in McKinney 2006a). Thus, during the simulation the 3-velocity in the equatorial plane is set to agree with this condition. Such a 3-velocity is generally time-like for points between the inner and outer light “cylinders,” but outside this region the 3-velocity can be space-like and so unphysical. In the event that the 3-velocity is space-like, the Lorentz factor is constrained to a fixed large value as described in section 2.5 of McKinney (2006a). This safety feature is necessary to handle the violent evolution seen early in the simulations, but it is not activated after the solution approaches a stationary state.

In the work described here, the initial conditions of the simulations are chosen to correspond to a non-rotating, current-free (except at the equator) force-free solution with $B^\phi = 0$. For example, for the paraboloidal models, BZ’s paraboloidal solution with $a/M = 0$ is used to set the initial conditions. For other power-law current profiles (e.g., $\nu = 3/4$), McKinney & Narayan (2006) describe how to calculate analytic solutions to the non-rotating problem. During the time evolution, B^θ at the disk is held fixed at its initial value, and the field angular velocity Ω_F is set to a physically motivated profile as suggested by the GRMHD models (McKinney & Narayan 2006). For models with rotating disks and/or rotating black holes, the initial non-rotating state is far from the steady state solution, so the model undergoes violent non-stationary evolution. Eventually, however, it relaxes to a steady-state solution. All solutions thus found are necessarily stable to Eulerian axisymmetric perturbations.

2.2 Modelling the Transition Region

The transition region between the disk and the black hole must be treated carefully to avoid undesirable discontinuities in the magnetosphere away from the equatorial disk. We now discuss how the vector potential (A_ϕ , which is used to obtain B^θ) and the field angular frequency (Ω_F) are chosen.

2.2.1 Softened Vector Potential

If one uses an arbitrary vector potential to set the profile of $B^\theta(r)$ at the disk, then this boundary condition may not

always allow for a stationary solution or one without discontinuities. The problem is that we calculate B^θ from the vector potential (A_ϕ) for an idealized problem with $a/M = 0$ or even $M = 0$, since these solutions are easy to obtain analytically. The solutions typically consist of power-law profiles. However, for general $M \neq 0$ and $a/M \neq 0$, the radial eigenfunctions must change character near the black hole in such a way that the solution for the vector potential must become nearly constant close to the horizon.

This property of the force-free equations near the horizon is related to the fact that solutions have a minimal energy if the black hole has a minimal tangential field on the horizon (Thorne & MacDonald 1982a; MacDonald & Thorne 1982b). For example, compared to the pure self-similar paraboloidal solution of Blandford (1976), BZ's paraboloidal solution for a disk around a black hole effectively softens the vector potential near the black hole to a monopolar form in order to account for the presence of the black hole. The characteristic radius where the change occurs in the case of a non-rotating hole is $r \sim 2r_g$. For rapidly rotating black holes the horizon becomes smaller but the ergospheric radius in the equatorial plane remains at $r = 2r_g$. So we expect generically that the softening of the potential will occur inside $r \sim 2r_g$ for all spins.

In our work, we take the analytic vector potential solution corresponding to $M = 0$, $a/M = 0$ and soften it by replacing the radial coordinate r as follows,

$$r \rightarrow (r^2 + r_{\text{transB}}^2)^{1/2}, \quad (2)$$

where r_{transB} is the transition radius. This allows the solution to become monopolar near the horizon, thus modeling the effects of the mass and spin of the black hole. Usually we set $r_{\text{transB}} = 2r_+$, but none of the results depend sensitively on this choice, as we have confirmed by trying various values in the range $r_{\text{transB}} = (1.5 - 4)r_g$.

2.2.2 Modelling the Angular Velocity

The simplest force-free solutions have no discontinuities except as defined by the boundary conditions. In time-dependent force-free simulations, discontinuities can appear near the boundary if no simple force-free solution exists with the chosen boundary condition. This is something to be avoided. Therefore, in order to guarantee a simple force-free solution, the boundary conditions must sometimes be modified to match smoothly onto the magnetosphere. Even in quasi-analytic work it is useful to avoid discontinuities in the transition from the boundary conditions to the magnetosphere (Uzdensky 2004, 2005).

In our models, the transition region where the disk meets the horizon requires careful treatment of the boundary condition in the disk. This is where the field line rotation switches from the profile set by the disk to the value required by the black hole space-time. We have tried two different models of the transition region. In one model, we take the field angular velocity profile to be given by

$$\Omega_F = \begin{cases} \Omega_{\text{DBH}}, & r < r_{\text{trans}\Omega}, \\ \Omega_K \left(1 - \left(\frac{r_+}{r}\right)^3\right) + \Omega_{\text{DBH}} \left(\frac{r_{\text{trans}\Omega}}{r}\right)^{n_t}, & r > r_{\text{trans}\Omega}. \end{cases} \quad (3)$$

The quantity Ω_{DBH} denotes the value of Ω_F on the black

hole horizon. We choose n_t so that there is a smooth transition. This model only applies for $a/M \geq 0$, and we find that values of $r_{\text{trans}\Omega}$ in the range from r_+ to $2r_+$ give acceptable results.

A second transition model is chosen to enforce Ω_F to be strictly constant inside the horizon and strictly fixed to the disk profile beyond some transition radius. This model is given by

$$\Omega_F = \begin{cases} \Omega_{\text{DBH}}, & r < r_0, \\ \Omega_{\text{DBH}} + A(r - r_0) + B(r - r_0)^3, & r_0 \leq r \leq r_{\text{trans}\Omega}, \\ \Omega_{\text{disk}}, & r > r_{\text{trans}\Omega}, \end{cases} \quad (4)$$

where Ω_{DBH} again denotes the value of Ω_F at the black hole horizon. The values of A and B are chosen such that Ω_F and $d\Omega_F/dr$ are continuous at r_0 and $r_{\text{trans}\Omega}$, where both radii are arbitrarily chosen. This model is suitable for any value of a/M .

As in BZ77, we assume that on the horizon ($r = r_+$) the angular frequency of field lines that thread the disk match onto some *fraction* of the black hole angular frequency

$$\Omega_H \equiv \frac{a}{2r_+}. \quad (5)$$

This matching of Ω_F between the disk and the magnetosphere of the black hole enforces the condition that no extra surface currents (i.e., jumps in the field) are present that would have been created by a jump in the field angular frequency at the interface between the disk and black hole magnetosphere. To find force-free solutions with no discontinuities, we iteratively repeat the simulations with improved values of Ω_{DBH} until the solution has a minimal discontinuity.

3 BZ PARABOLOIDAL SOLUTION

In this section the GRFFE equations of motion are self-consistently evolved to find the stationary force-free magnetospheric solution corresponding to the toroidal current distribution of the paraboloidal solution of Blandford & Znajek (1977), viz.,

$$\frac{dI_\phi}{dr} = \frac{C}{r^{2-\nu}}, \quad (6)$$

with $\nu = 1$.

In the absence of rotation, the vector potential for the paraboloidal solution takes the form

$$A_\phi^{(\text{para})} = \begin{cases} +g(r, \theta) & \theta < \pi/2 \\ +g(r, \pi - \theta) & \theta > \pi/2, \end{cases} \quad (7)$$

$$g(r, \theta) \equiv \frac{C}{2}[rf_- + 2Mf_+(1 - \ln f_+)], \quad (8)$$

where $f_+ = 1 + \cos\theta$, $f_- = 1 - \cos\theta$, and M is the mass of the black hole. As explained earlier, this non-rotating solution is used as the initial conditions for rotating models, i.e., we obtain the boundary condition on the field at the equatorial plane from the non-rotating solution, viz., $B^\theta = -A_\phi/r/\sqrt{-g}$, and we hold this fixed for all time. We set $C = 1$ throughout the paper, and this normalizes all energy densities and field strengths.

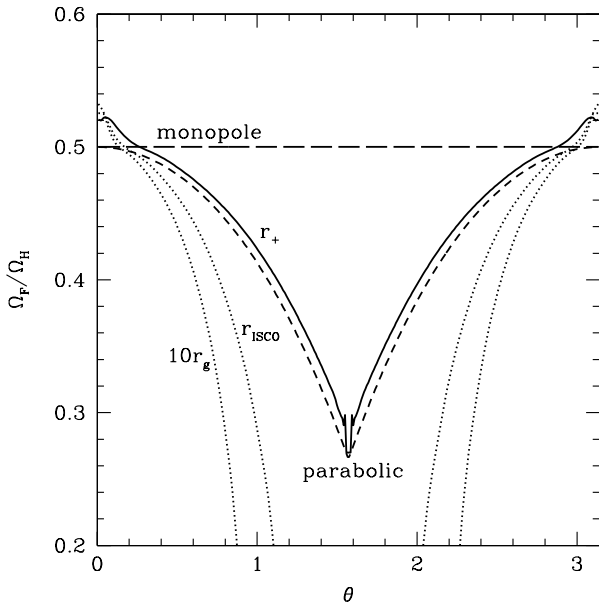


Figure 1. Field angular frequency per unit black hole angular frequency (Ω_F/Ω_H) vs. θ in radians on the horizon ($r = r_g$, solid line) and at two other radii ($r = r_{\text{ISCO}} \approx 5.997r_g$ and $r = 10r_g$, dotted lines). The results correspond to a GRFFE simulation of the paraboloidal solution ($\nu = 1$) at time $t = 1200t_g$ for a non-rotating disk and a slowly spinning black hole with $a/M = 0.001$. Also shown are the Blandford-Znajek monopole solution (long-dashed line) and paraboloidal solution (short-dashed line) on the horizon. Note the excellent agreement between the GRFFE numerical solution and BZ’s analytical model.

The BZ paraboloidal solution is based on the non-gravitational solution found initially by Blandford (1976). BZ hypothesized that the solution for the poloidal field is independent of the velocity profile of the disk (see eq. 3.10 in that paper). Blandford (1976) noted in section 3iii that gravity will add corrections but, in fact, even without gravity there are corrections for any significant amount of disk rotation. Keplerian disks in particular have substantially different solutions from the non-rotating case since the Keplerian speed is a non-negligible fraction of the speed of light near the black hole. In the discussion that follows, we show that the Blandford (1976) and BZ solution for Ω_F and the energy output only applies when the disk is slowly rotating. We then calculate the correct solution for Ω_F and the power output for a Keplerian disk for the case of both slowly and rapidly rotating black holes.

We model the transition region using equation (4) with $r_0 = r_+$ and $r_{\text{trans}\Omega} = 2r_+$. We have also tried $r_{\text{trans}\Omega} = 1.2r_+$ and we find only small quantitative differences, though there are additional surface currents in the equatorial regions near the horizon because of the sharper transition in the Ω_F profile.

3.1 Slowly Rotating BH and Non-Rotating Disk

The first numerical model we describe has $a/M = 0.001$, i.e., a very slowly rotating black hole, and we assume a non-rotating disk, $\Omega_{\text{disk}} = 0$. We choose $\Omega_{\text{DBH}} = 0.27\Omega_H$ as in

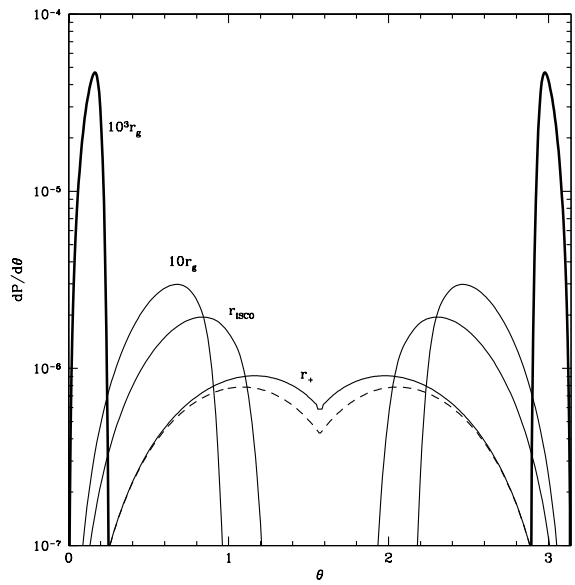


Figure 2. Angular density of the electromagnetic power output ($dP/d\theta$) vs. θ in radians at four radii, $r = \{r_+, r_{\text{ISCO}}, 10r_g, 10^3r_g\}$. The results are for the same GRFFE simulation shown in Figure 1. The dashed line shows the analytic solution for the power output at the horizon according to the BZ paraboloidal model. Note the excellent agreement between the numerical GRFFE result and BZ’s analytical model.

the BZ solution. Figure 1 shows Ω_F/Ω_H for the converged steady state solution at time $t = 1200t_g$ at three different radii: the horizon at $r = r_+$, the inner-most stable circular orbit (ISCO) at $r = r_{\text{ISCO}}$, and $r = 10r_g$. For comparison, the monopole and paraboloidal solutions on the horizon are also shown.

The profile of Ω_F/Ω_H from the numerical solution is very close to the analytical BZ solution. The small offset is due to our model of the transition region, where one would expect to obtain BZ’s solution only if allowing a discontinuity at the horizon as in their solution. There is a small residual jump near the equator in Ω_F due to not choosing the most optimal value for Ω_F on the horizon. Also, close to the poles Ω_F/Ω_H deviates from the expected value of $\Omega_F/\Omega_H \approx 1/2$ due to the coordinate singularity, though this feature has a negligible impact on the solution at large radii due to the collimation of field lines toward the polar axis.

Figure 2 shows the angular density of the electromagnetic power output

$$\left\langle \frac{dP}{d\theta} \right\rangle = 2\pi r^2 \left\langle -T^{(EM)t}_t \right\rangle, \quad (9)$$

where $-T^{(EM)t}_t$ is written in a coordinate basis in Boyer-Lindquist or Kerr-Schild coordinates. The total integrated electromagnetic power at radius r is obtained by integrating over angle,

$$P = \int_0^\pi \frac{dP}{d\theta} \sin\theta d\theta. \quad (10)$$

The integrated electromagnetic power output at each of the four radii, $r = \{r_+, r_{\text{ISCO}}, 10r_g, 10^3r_g\}$, is $P =$

$\{1.4, 1.6, 1.6, 1.6\} \times 10^{-6}$, respectively, in units in which the radial field on the horizon at the poles is unity; that is, we scale the power as $(dP/d\theta)/B_0^2$ and P/B_0^2 , where B_0 is the radial field strength on the horizon at the polar axis at the end of the simulation. Normalized in the same way, BZ's paraboloidal solution gives a power of $P \approx 1.2 \times 10^{-6}$ on the horizon (Blandford & Znajek 1977). Clearly, our numerical solution is in good agreement. The small differences arise because our numerical solution for Ω_F is slightly larger and the power on the horizon scales as $P \propto \Omega_F(\Omega_F - \Omega_H)$. We find that along field lines the value of Ω_F is constant to within 5%, as required for an axisymmetric, stationary solution.

Figure 2 shows that the numerical profile for the angular power density agrees well with the analytical BZ solution. The slight difference is due to the introduction of the transition region between the disk and black hole. Note that the power becomes progressively more collimated with increasing radius. The peak in the power density lies at only $\theta \approx 10^\circ$ by a radius of $r = 10^3 r_g$.

One can also compute the average efficiency ($\bar{\epsilon}$) over the horizon, following equation 7.6 in Blandford & Znajek (1977):

$$\bar{\epsilon} = \frac{\int_0^\pi \sin \theta d\theta \left(\frac{dP}{d\theta} \right)}{\int_0^\pi \sin \theta d\theta \left(\frac{dP}{d\theta} \right) \left(\frac{\Omega_H}{\Omega_F} \right)}. \quad (11)$$

Effectively, this is an estimate of Ω_F/Ω_H , weighted by the power density. This quantity has a maximum value of 50% for the monopolar solution. Our numerical solution gives an efficiency of 39%, which is similar to the value of 38% for the analytical BZ paraboloidal solution.

In summary, the GRFFE numerical solution for the force-free magnetosphere surrounding a slowly-spinning black hole and a non-rotating disk agrees well with the analytical solution of BZ.

3.2 Slowly Rotating Black Hole and Keplerian Disk

We now describe a second numerical GRFFE model, which is identical to the previous model except now the disk rotates at the Keplerian frequency, $\Omega_{\text{disk}} = \Omega_K = 1/(r^{3/2} + a)$ in Boyer-Lindquist coordinates. Because the Keplerian speed near the black hole is much larger than the black hole rotation speed, it leads to significant changes in the field around the horizon. The transition from the Keplerian disk to the relatively slow black hole speed forces the electromagnetic energy to be accreted rather than extracted from the black hole. The integrated electromagnetic power output at the radii $r = \{r_+, r_{\text{ISCO}}, 10r_g, 10^3 r_g\}$ is $P = \{-0.001, 0.36, 1.42, 2.04\}$, respectively, in the same units as before. For such slowly spinning black holes with rapidly rotating disks, the power output on the horizon depends sensitively on how we model the transition region between the disk and black hole. In particular, the negative power on the horizon results from a complicated set of currents in the magnetosphere that provide a black hole-disk connection. The substantial power at large radii primarily reflects the power output of the rotating disk and there is very little power from the black hole itself. For all attempted models

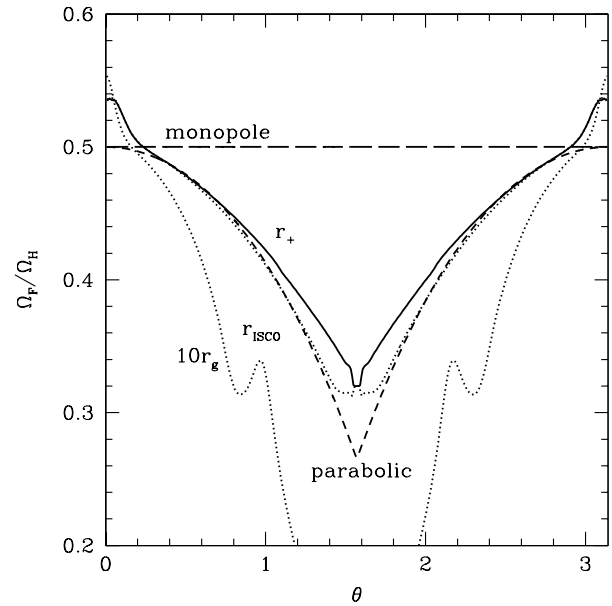


Figure 3. Field angular frequency per unit black hole angular frequency (Ω_F/Ω_H) vs. θ in radians on the horizon ($r = r_g$, solid line) and at two other radii ($r = r_{\text{ISCO}} \approx 2.321r_g$ and $r = 10r_g$, dotted lines). The results correspond to the paraboloidal solution ($\nu = 1$) at time $t = 1200t_g$ for a Keplerian disk around a rapidly spinning black hole with $a/M = 0.9$. Also shown are the Blandford-Znajek monopole solution (long-dashed line) and paraboloidal solution (short-dashed line) on the horizon. The agreement between the numerical GRFFE model and the analytical BZ model is not as good as for a slowly rotating black hole (Figure 1), but the deviations are still fairly mild.

of the transition region, we find additional surface currents in the magnetosphere above the disk.

3.3 Rapidly Rotating BH and Keplerian Disk

Finally, we consider a rapidly rotating black hole with $a/M = 0.9$, surrounded by a Keplerian disk ($\Omega_{\text{disk}} = \Omega_K$). If we directly use BZ's paraboloidal solution for a slowly rotating BH to setup the disk boundary condition for the currents, only for $a/M \ll 1$ were we able to find a solution without discontinuities near the horizon. In order to account for the additional effects of rapid spin, we had to soften the vector potential by replacing the radial coordinate as described in equation (2). This was not required for slowly spinning models.

With this model of the transition region we were able to find a solution with $\Omega_{\text{DBH}} = 0.32\Omega_H$, which is a slightly larger value than for BZ's paraboloidal solution for a slowly spinning black hole. Figure 3 shows Ω_F/Ω_H at $t = 1200t_g$ at three different radii and also shows the monopole and paraboloidal solutions on the horizon for comparison.

Figure 4 shows the angular density of the power output. The peak in the power density occurs at a half-opening angle of 9° – 14° at a radius of $r = 10^3 r_g$. The integrated electromagnetic power output at radii $r = \{r_+, r_{\text{ISCO}}, 10r_g, 10^3 r_g\}$ is $P = \{0.48, 0.57, 1.39, 1.77\}$, respectively. Clearly, there is a non-negligible power output from the black hole and the transition region between the horizon and the ISCO. There

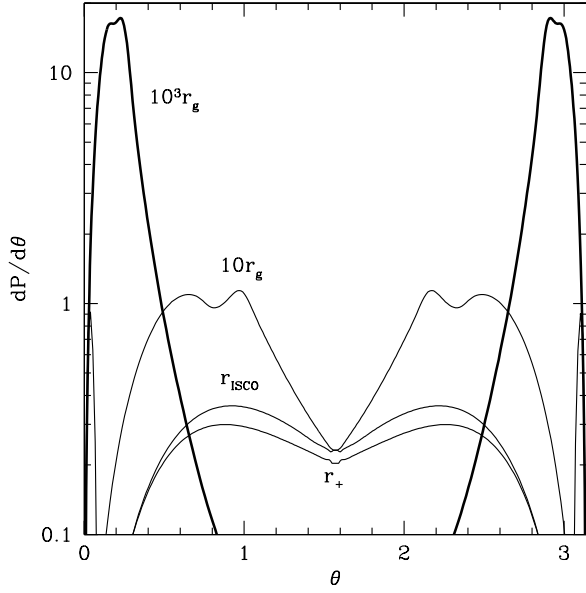


Figure 4. Angular density of the electromagnetic power output ($dP/d\theta$) vs. θ in radians at four radii, $r = \{r_+, r_{\text{ISCO}}, 10r_g, 10^3r_g\}$, for the GRFFE solution shown in Figure 3. The power is collimated within a half-opening angle of 9° – 14° by $r = 10^3r_g$.

is substantial power from the disk as well. From equation (11), the average efficiency is 41% for this model, which has a rapidly rotating black hole. It is slightly higher than in the original BZ model for a slowly spinning black hole.

Figure 5 shows the structure of the magnetosphere once the solution has reached a stationary state. As in the paraboloidal solution of Blandford-Znajek, the field geometry becomes monopolar near the horizon. This general relativistic effect becomes prominent once the field lines thread the ergosphere.

Now we consider the radial dependence of certain quantities along a field line starting at $\theta \approx 60^\circ$ on the horizon out to large radii. The half-opening angle of the field line is found to follow

$$\theta_j \approx 54^\circ \left(\frac{r}{2.8r_g} \right)^{-0.48}, \quad (12)$$

which is close to the scaling $\theta_j \propto r^{-1/2}$ for the non-rotating $\nu = 1$ paraboloidal solution (McKinney & Narayan 2006). The field has apparently slightly decollimated compared to the non-rotating case, which is also clear from Figure 6 where the field lines in the rotating model are seen to be slightly decollimated with respect to the nonrotating solution. Thus it appears that the decollimating centrifugal force associated with rotation is somewhat stronger than the collimating hoop-stresses associated with the toroidal field generated by rotation.

For a force-free solution, the minimum Lorentz factor with which observer at infinity would see particles moving is given by the drift speed. At large radii this minimum Lorentz factor is well-fitted by

$$\Gamma \equiv u^t \sqrt{-g_{tt}} \approx 1.5 \left(\frac{r}{42.5r_g} \right)^{0.55}, \quad (13)$$

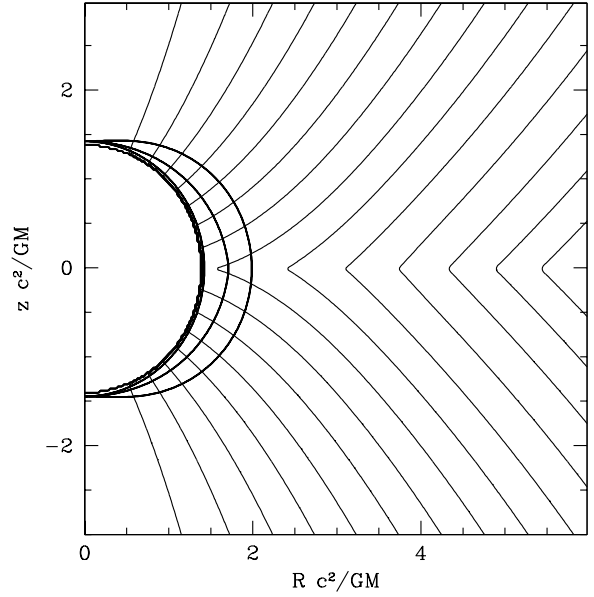


Figure 5. For the paraboloidal ($\nu = 1$) model with $a/M = 0.9$ and a Keplerian disk, this shows the poloidal field geometry given by contours of the vector potential (A_ϕ). Also shown, from inner to outer radius, are the inner-radial computational boundary, horizon at $r = 1 + \sqrt{1-a^2}$, the inner “light cylinder” corresponding to the Alfvén surface for ingoing Alfvén waves, and the ergosphere at $r = 1 + \sqrt{1-(a \cos \theta)^2}$. Notice that the field geometry becomes monopolar near the horizon as in the original Blandford-Znajek solution.

which is similar to the scaling $\Gamma \propto r^{1/2}$ found by Beskin & Nokhrina (2006) for paraboloidal MHD models. This suggests that the force-free flow may be a good model of the acceleration regime in GRMHD models, at least at those radii where the magnetic energy is much larger than the kinetic energy.

The orthonormal toroidal field at large radii follows

$$B^{\hat{\phi}} \approx B^\phi \sqrt{g_{\phi\phi}} \approx 0.26 \left(\frac{r}{r_g} \right)^{-0.6}, \quad (14)$$

and the pitch angle at large radii follows

$$\alpha_{\text{pitch}} \equiv \tan^{-1} \left(\frac{B^{\hat{r}}}{B^{\hat{\phi}}} \right) \approx \tan^{-1} \left(\frac{c}{\sqrt{g_{\phi\phi}} \Omega_F} \right), \quad (15)$$

where the speed of light (c) has been temporarily reintroduced. This is consistent with an orthonormal radial field of the form

$$B^{\hat{r}} \approx -\frac{c}{\Omega_F \sqrt{g_{\phi\phi}}} B^{\hat{\phi}}, \quad (16)$$

which is a generic feature of force-free solutions with rotating field lines (see equation (A8) in Appendix A). Studies of stability suggest that force-free fields that follow the above behavior are stable to the nonaxisymmetric kink instability (Tomimatsu et al. 2001), though our axisymmetric simulations cannot test this.

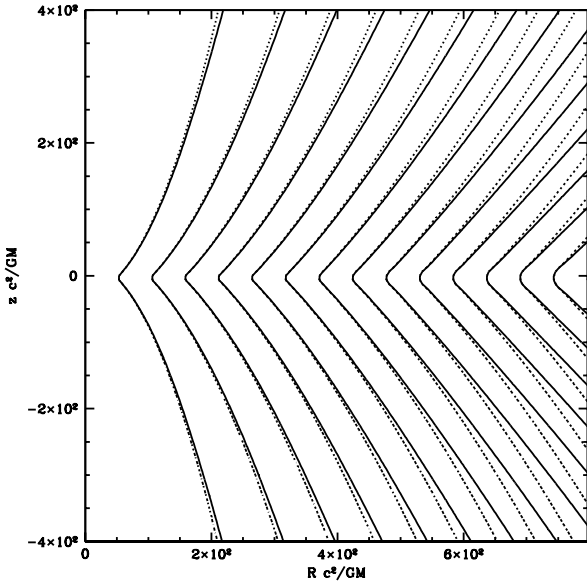


Figure 6. Field lines (constants of A_ϕ) for the $a/M = 0.9$ paraboloidal ($\nu = 1$) model at $t = 0$ (initial state, non-rotating solution, dotted lines) and $t = 1.2 \times 10^3 t_g$ (final time, converged rotating solution, solid lines). The field is seen to decollimate slightly in the presence of rotation, but the effect is quite mild. Slower and more rapidly rotating black holes show similar results.

3.4 Summary of Paraboloidal Solutions

The original BZ paraboloidal solution could not describe the transition region between the accretion disk and black hole, it does not account for modification of the field direction for disks with Keplerian rotation profiles, and it only applies to slowly spinning black holes. Our numerical work has eliminated these restrictions. For rapidly rotating black holes, we find an enhanced averaged efficiency for the power from the black hole. We find that power output from the transition region between the disk and black hole contributes a significant fraction of the total power output from the system. We find that for slowly spinning black holes the transition region is important in determining force balance and the power output on the horizon.

4 GRMHD-MOTIVATED $\nu = 3/4$ SOLUTION

Since GRMHD numerical models produce disk currents consistent with a $\nu = 3/4$ distribution (McKinney & Narayan 2006), we now focus on force-free solutions with this scaling for the current. In this section we describe the model of the toroidal current and the field rotation frequency as deduced from GRMHD simulations, and we study corresponding GRFFE numerical models to determine the power and collimation of the Poynting-dominated jet and electromagnetic disk wind.

4.1 Current Model

The initial conditions are chosen to be the non-rotating flat-space ($M = a/M = 0$) $\nu = 3/4$ model described in

McKinney & Narayan (2006). The vector potential is given by

$$A_\phi = Cr^\nu |\sin \theta| P_{\nu-1}^1(\cos \theta), \quad (17)$$

where P_l^m is the associated Legendre function of the first kind. For the case of interest, viz., $\nu = 3/4$, the angular solution takes the form P_l^m with $l = -1/4$ and $m = 1$. We set $C = 1$ throughout the paper, and this normalizes all energy densities and field strengths. As in the case of the paraboloidal models, this vector potential is used to obtain the boundary condition on B^θ at the disk, which is then held fixed for all time. We modify the self-similar solution to account for the transition region near the black hole via the mapping given in equation (2). The main effect of this smoothing operation near the black hole is the introduction of a split-monopole field near the center. As found in McKinney & Gammie (2004) and McKinney (2006c), the field is indeed nearly monopolar across the horizon in the Poynting-dominated jet region. This is consistent with the fact that all force-free solutions with $M \neq 0$ tend to become monopolar near the horizon.

4.2 Field Rotation Model

We use GRFFE numerical models to investigate the two models of Ω_F described in equations (3) and (4). For the latter, we choose $\Omega_{\text{disk}} = \Omega_K$, $r_0 = 2r_+$ and $r_{\text{trans}\Omega} = 3r_+$, though we have found that choosing $r_0 = r_+$ and $r_{\text{trans}\Omega} = 2r_+$ leads to only small quantitative differences. To fit the time-averaged GRMHD numerical model shown in Figure 8 in McKinney & Narayan (2006), one could choose $\Omega_{\text{DBH}} = 0.6\Omega_H$. For general a/M , a good fit is provided by $\Omega_{\text{DBH}} \sim \Omega_H/2$ for $a/M \gtrsim 0.4$ and $\Omega_{\text{DBH}} = \Omega_H$ for slower black hole spins (McKinney & Narayan 2006). Note that Ω_F is the same in Kerr-Schild and Boyer-Lindquist coordinates, and Ω is also the same at the equator. Thus, the above prescription for Ω_F in the equatorial disk is valid for both coordinate systems.

4.3 Rotating Black Hole and a $\nu = 3/4$ Keplerian Disk

We consider a GRFFE model with a black hole spin of $a/M = 0.9$ and an equatorial current sheet with a $\nu = 3/4$ power law current distribution. Our fiducial model for the transition region, called “TModel 1,” smooths the field vector potential using equation (2) with $r_{\text{transB}} = 2r_+$, and models the field rotation via equation (3) with $\Omega_{\text{DBH}}/\Omega_H = 0.32$ and $r_{\text{trans}\Omega} = 2r_+$.

For this transition model we seek to find force-free solutions with no discontinuities. If one chooses $\Omega_{\text{DBH}} = 0.6\Omega_H$ as in the GRMHD simulations, discontinuities appear above the equatorial plane. This is expected since the disk is not force-free. The value $\Omega_{\text{DBH}} = 0.32\Omega_H$ was chosen to give a smooth transition from the disk to the black hole so that there are negligible discontinuities near the accretion disk - black hole interface that would correspond to extra toroidal currents in the magnetosphere. Other transition models are considered in section 4.5, such as one where we do choose $\Omega_{\text{DBH}} = 0.6\Omega_H$ and allow discontinuities to be present in the magnetosphere.

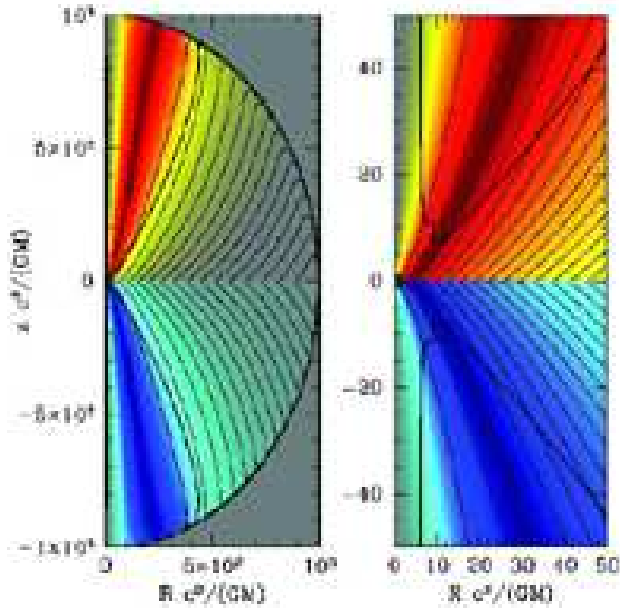


Figure 7. Field lines (black lines), enclosed poloidal current (B_ϕ , where $B_\phi \approx B^\phi \sqrt{g_{\phi\phi}}$, red positive, blue negative), and light “cylinder” (thick black line). The results correspond to a GRFFE model with $\nu = 3/4$ at time $t = 1200t_g$ for a rotating disk around a spinning black hole with $a/M = 0.9$. The panel on the left shows the full computational domain and that on the right shows a closeup of the central region. The black hole and the disk together generate a Poynting outflow in the form of a jet surrounded by a wind, with power focused along the polar axis. Small artifacts at the outer radial edge in the left panel are the result of interpolation and reflections of the Poynting jet off the outer radial boundary.

Starting with the non-rotating force-free solution as initial conditions, the above model was simulated with the GRFFE code until it reached steady state ($t = 1200t_g$). Figure 7 shows the poloidal structure of field lines (also lines of constant A_ϕ), the enclosed poloidal current from the pole (B_ϕ), and the light “cylinders” (only the outer light cylinder is clearly visible) in the final state. The poloidal field geometry has changed little from the initial solution, showing that rotation has a negligible effect. The polar enclosed poloidal current (B_ϕ) is shown in color, where the radial energy flux is given by $F_E^r = \Omega_F B_\phi B^r$. Note that for stationary, axisymmetric flows B_ϕ and Ω_F are constant along field lines.

The field lines in the $\nu = 3/4$ solution show less poloidal collimation than the paraboloidal solution but more than the monopole solution (which has no collimation at all). As compared to the GRMHD solution, the pressure support of the corona has been replaced by the stable force-free field lines, but otherwise the funnel region is quantitatively similar to the GRMHD solution.

Figure 8 shows the structure of the magnetosphere once the solution has reached a stationary state. As in the paraboloidal solution described previously, the field geometry becomes slightly monopolar near the horizon. This general relativistic effect becomes important once the field lines thread the ergosphere.

Figure 9 diagnoses the poloidal current flow and angular

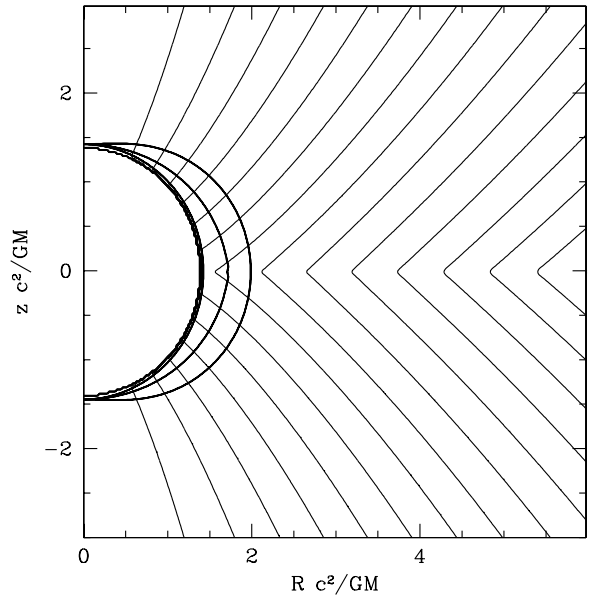


Figure 8. Similar to Figure 5, but for the GRMHD-motivated, $a/M = 0.9$, Keplerian disk model with a $\nu = 3/4$ current distribution. Notice that the field geometry becomes slightly monopolar near the horizon.

rotation of field lines in the force-free magnetosphere at a radius of $r = 20$. The value of B_ϕ is the amount of poloidal current enclosed away from the polar axis down to the given value of A_ϕ , where $A_\phi = 0$ on the polar axis. This plot shows that there is an increase in current away from the polar axis due to the jet coming from the black hole, and then there is a drop in current as the disk supplies the return current. At large radii (large A_ϕ) the current vanishes. The current closes at $r = 0$ and $r = \infty$ in a non-singular manner, unlike in the paraboloidal case where B_ϕ is finite at large radii so that the radially integrated poloidal current is infinite. The small-scale oscillation in B_ϕ is located at the black hole jet-disk interface, and the detailed behavior of this region depends on the black hole spin and disk rotation profile. This current structure is comparable to that of neutron star magnetospheres (see, e.g. McKinney 2006b). The plot also shows Ω_F/Ω_H as a function of A_ϕ . This shows how the black hole solution at small A_ϕ matches onto the Keplerian disk at large A_ϕ .

4.3.1 Angular Dependence within Jet

Figure 10 shows Ω_F/Ω_H for the $\nu = 3/4$ solution at $t = 1200t_g$ at three different radii and also shows the monopole and paraboloidal solutions on the horizon. As expected, the $\nu = 3/4$ solution has a field rotation at the horizon ($\Omega_F/\Omega_H \approx 0.32$) that is close to the paraboloidal solution ($\nu = 1$, $\Omega_F/\Omega_H \approx 0.32$ for $a/M = 0.9$) and lower than the monopole solution ($\nu = 0$, $\Omega_F/\Omega_H \approx 0.5$). The profile of Ω_F/Ω_H is similar to the GRMHD models shown in Figure 8 (left panel) in McKinney & Gammie (2004). In their plot the value of $\Omega_F/\Omega_H \approx 0.32$ near the transition between the force-free region and the accretion disk region. This is further evidence that the $\nu = 3/4$ GRFFE model gives a

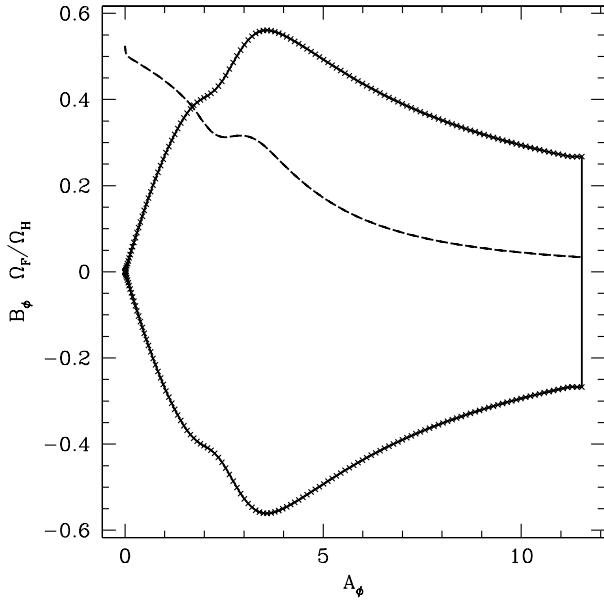


Figure 9. Enclosed poloidal current (B_ϕ , where $B_\phi \approx B^{\hat{\phi}} \sqrt{g_{\phi\phi}}$, solid line with crosses) and field angular frequency per unit black hole angular frequency (Ω_F/Ω_H , dashed line) vs. the vector potential ($A_\phi = \Psi$, also called the flux function) at spherical polar radius $r = 20$. This shows that the poloidal current increases in the jet and then decreases at larger radii in the disk that contributes to a line return current. There is no enclosed current at $r = \infty$ unlike in the paraboloidal case. This also shows how the rotation frequency of the field lines behaves near the black hole and how it connects onto the Keplerian disk at large radii (large A_ϕ).

solution that is consistent with the Poynting-dominated jet found in full GRMHD. Close to the poles Ω_F/Ω_H deviates from the expected value of $\Omega_F/\Omega_H \approx 1/2$ due to the coordinate singularity. However, this feature has negligible impact on the solution at large radii due to the collimation of field lines toward the polar axis.

Figure 11 shows the angular density of the power output. The $\nu = 3/4$ disk provides most of its energy inside $r = 100r_g$. The integrated electromagnetic power output at $r = \{r_+, r_{\text{ISCO}}, 10r_g, 10^3r_g\}$ is $P = \{0.47, 0.62, 1.50, 1.76\}$, respectively. The figure shows that the peak in the power is collimated to within a half-opening angle of 15° – 26° by $r = 10^3r_g$. Using equation (11), we calculate an average efficiency of 41% for this model, which is the same as the equivalent paraboloidal model.

One can compare the electromagnetic power outputs in the GRFFE model to those found in the equivalent GRMHD model discussed in McKinney & Narayan (2006). The powers are comparable at the horizon. However, in the GRMHD model, the electromagnetic power from the disk is lost to the matter and only the power from the black hole survives at large radii, whereas in the GRFFE model all the electromagnetic power output of the black hole and the disk reaches large radii.

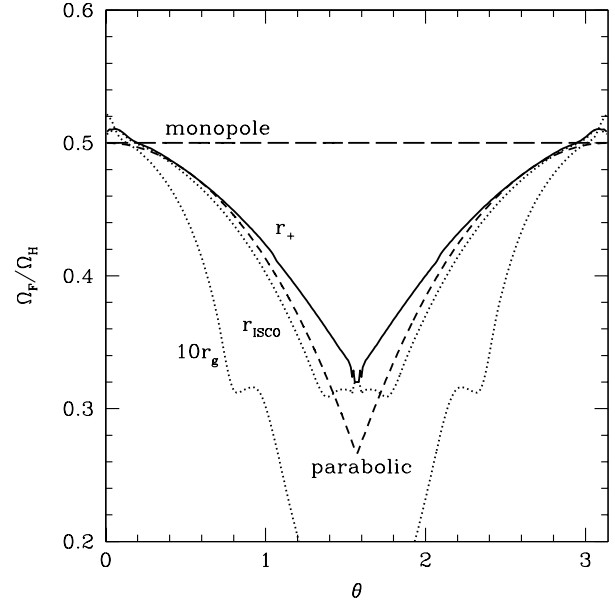


Figure 10. Field angular frequency per unit black hole angular frequency (Ω_F/Ω_H) vs. θ in radians on the horizon ($r = r_g$, solid line) and at two other radii ($r = r_{\text{ISCO}} \approx 2.3209r_g$ and $r = 10r_g$, dotted lines). The results correspond to a GRFFE model with $\nu = 3/4$ at time $t = 1200t_g$ for a rotating disk around a spinning black hole with $a/M = 0.9$. Also shown are the Blandford-Znajek monopole solution (long-dashed line) and paraboloidal solution (short-dashed line) on the horizon. Note that the field angular frequency at the horizon is roughly similar for the paraboloidal ($\nu = 1$) and $\nu = 3/4$ models.

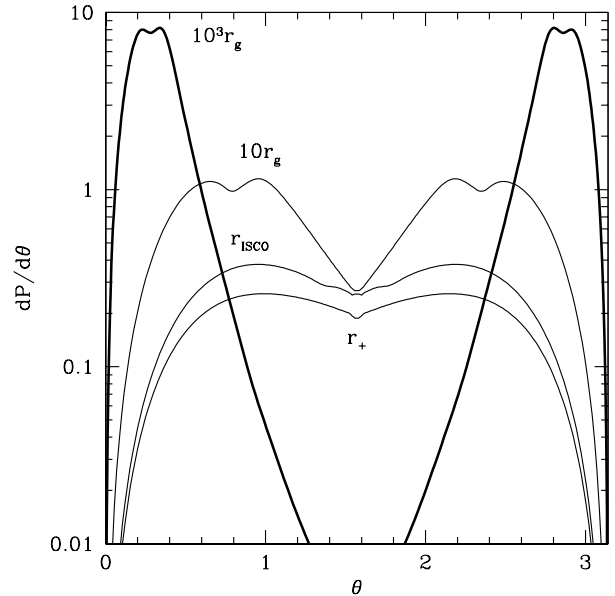


Figure 11. Angular density of the electromagnetic power output ($dP/d\theta$) vs. θ in radians at four radii, $r = \{r_+, r_{\text{ISCO}}, 10r_g, 10^3r_g\}$, for the GRFFE solution shown in Figure 10. The power is seen to be collimated within a half-opening angle of 15° – 26° by $r = 10^3r_g$. The collimation is significantly less than in the otherwise similar paraboloidal ($\nu = 1$) model.

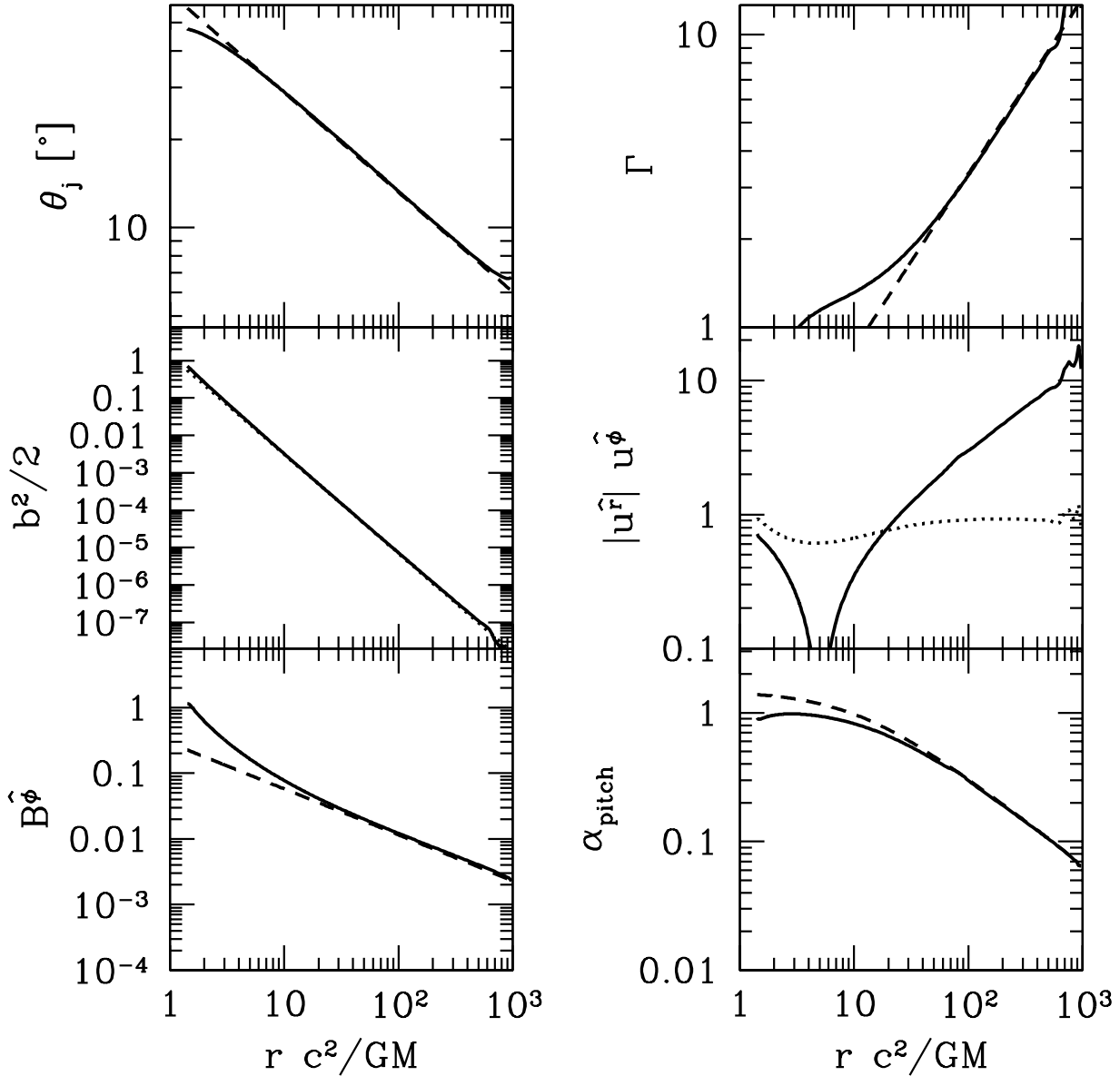


Figure 12. Variation with radius of various quantities in the converged GRFFE solution with $\nu = 3/4$ and a rotating disk around a spinning black hole with $a/M = 0.9$. The solid lines in the panels show the half-opening angle of the jet in degrees (θ_j), the Lorentz factor (Γ), the comoving energy density ($b^2/2$), the orthonormal radial velocity ($u^{\hat{r}}$), the orthonormal toroidal field strength ($B^{\hat{\phi}}$), and the pitch angle in radians (α_{pitch}). The features near the outer radial boundary are due to reflections of initial transients off the boundary. Except for the panel with α_{pitch} , the dashed lines in the other panels show power-law fits to the numerical results. The dotted line in the $u^{\hat{r}}$ panel shows the orthonormal angular velocity $u^{\hat{\phi}}$. The dashed line in the α_{pitch} panel shows the limit below which the kink instability will be present according to Tomimatsu et al. (2001). It indicates that the flow is marginally stable at large radii. The other panels show that the solution has a power-law behavior at large radii.

4.3.2 Radial Dependence within Jet

Figure 12 shows the jet half-opening angle (θ_j), the Lorentz factor ($\Gamma \equiv u^t \sqrt{-g_{tt}}$), the comoving energy density ($b^2/2$), the approximate orthonormal absolute value of radial and ϕ velocities ($|u^{\hat{r}}| \equiv |u^r| \sqrt{g_{rr}}$ and $u^{\hat{\phi}} \equiv u^{\phi} \sqrt{g_{\phi\phi}}$), the orthonormal toroidal field strength ($B^{\hat{\phi}} \equiv B^{\phi} \sqrt{g_{\phi\phi}}$), and the

pitch angle within the jet ($\alpha_{\text{pitch}} \equiv \tan^{-1}(B^{\hat{r}}/B^{\hat{\phi}})$). The figure also shows power-law fits to some quantities. This figure can be compared to panels in figures 7 and 8 in McKinney (2006c).

The opening angle of the jet for the field line starting at $\theta_j \approx 57^\circ$ has a power-law dependence at large radii that

follows

$$\theta_j \approx 57^\circ \left(\frac{r}{2.8r_g} \right)^{-0.34}, \quad (18)$$

compared to $\theta_j \propto r^{-0.375}$ for the non-rotating $\nu = 3/4$ solution (McKinney & Narayan 2006). This shows that the field has slightly decollimated compared to the non-rotating solution, but the effect is weak. The power-law dependence for θ_j is strikingly similar to that found for the opening angle of the jet in GRMHD simulations given by equations (24) and (25) in McKinney (2006c). For example, the choice of $\theta_j \approx 57^\circ$ on the horizon for the field line corresponds to where the Poynting-dominated jet starts in the GRMHD simulations of McKinney (2006c) and corresponds to where the combined disk+corona scale height to radius ratio is $H/R \approx 0.6$. In this force-free model, $\theta_j \approx 5^\circ$ at $r \approx 5 \times 10^3 r_g$, a similar value as found in McKinney (2006c) for the core of the jet at large radii.

The GRMHD simulations and the present force-free model have an opening angle that is consistent up to the point where in the GRMHD model the jet becomes conical due to dissipative processes. In the GRMHD simulations the power-law dependence slightly depends on the field line chosen, while in these GRFFE simulations the power-law dependence is the same for all field lines.

The Lorentz factor at large radii is well-fitted by

$$\Gamma \approx 2 \left(\frac{r}{42.5r_g} \right)^{0.6}, \quad (19)$$

which is consistent with the magnetic acceleration domain found in McKinney (2006c). This behavior is also similar to the analytic result of $\Gamma \propto r^{1/2}$ obtained by Beskin & Nokhrina (2006) for paraboloidal MHD winds.

As in the GRMHD model of McKinney (2006c), the plasma angular velocity ($u^{\hat{\phi}}$) remains subrelativistic while the radial velocity ($u^{\hat{r}}$) becomes relativistic.

The comoving energy density follows

$$\frac{b^2}{2} \approx 1.4 \left(\frac{r}{r_g} \right)^{-2.65}, \quad (20)$$

which is close to the scaling $b^2 \propto r^{-2.5}$ found for the non-rotating $\nu = 3/4$ solution. This implies that the black hole and disk rotation has only a small effect on the field energy.

The orthonormal toroidal field follows

$$B^{\hat{\phi}} \approx 0.29 \left(\frac{r}{r_g} \right)^{-0.7}, \quad (21)$$

which is remarkably close to the GRMHD solution found in McKinney (2006c) for the inner-radial region before dissipation becomes important at $r \sim 10^3 r_g$.

The pitch angle is found to follow

$$\alpha_{\text{pitch}} \approx \tan^{-1} \left(\frac{c}{g_{\phi\phi} \Omega_F} \right), \quad (22)$$

with the speed of light (c) temporarily reintroduced. As for the paraboloidal models, the orthonormal radial field at large radii is well-fitted by

$$B^{\hat{r}} \approx -\frac{c}{\Omega_F \sqrt{g_{\phi\phi}}} B^{\hat{\phi}}. \quad (23)$$

Summarizing this section, there are two main results. First, the poloidal structure of the field in the rotating

GRFFE models considered in this paper is rather similar to the field structure found in the non-rotating models discussed in McKinney & Narayan (2006). Since we showed previously that the latter models agree well with the poloidal field structure in the jet region of GRMHD models, the present models also agree well. Second, the structure of the toroidal field, along with various related quantities such as the pitch angle, Poynting flux, jet acceleration, Lorentz factor, etc., obtained from the rotating GRFFE solution agree very well with the corresponding quantities in the GRMHD jet. Thus, the rotating GRFFE model appears to be an excellent representation of all facets of jets.

4.3.3 Stability

The pitch angle of the magnetic field lines becomes progressively smaller at large distances, becoming as small as $\alpha_{\text{pitch}} \approx 3^\circ$ at $r = 10^3 r_g$. This is consistent with the Poynting-dominated jet studied in McKinney (2006c). The small pitch-angle argues that the flow might be kink unstable, since the Kruskal-Shafranov criterion for instability is abundantly satisfied. The criterion for instability is given by

$$\left| \frac{B^{\hat{\phi}}}{B^{\hat{r}}} \right| \gtrsim \frac{R}{L}, \quad (24)$$

where $L \approx \sqrt{g_{\theta\theta}}$ is approximately the vertical length of the jet and $R \approx \sqrt{g_{\phi\phi}}$ is approximately the cylindrical radial extent of the jet.

Tomimatsu et al. (2001) considered the effect of rotation on stability and found that a Poynting-dominated jet is kink unstable only if both the Kruskal-Shafranov criterion *and* the additional condition

$$\left| \frac{B^{\hat{\phi}}}{B^{\hat{r}}} \right| \gtrsim \frac{R}{R_L}, \quad (25)$$

is also satisfied, where $R_L = c/\Omega_F$ is the light cylinder radius (Tomimatsu et al. 2001). Their result only strictly applies inside the light cylinder and for a uniform field, but it does suggest that rotation could stabilize a jet that might appear unstable according to the Kruskal-Shafranov criterion. The lower right panel of Figure 12 compares the quantity $\tan^{-1}(R_L/\sqrt{g_{\phi\phi}})$ with the pitch angle, and suggests that the flow is marginally stable to the kink instability at large radii. Note, however, that the kink instability is non-axisymmetric, whereas our simulations are axisymmetric. Thus, 3D simulations are needed to check the Tomimatsu et al. (2001) stability analysis.

We can, however, study the stability of our numerical force-free solutions to the *axisymmetric* pinch instability both inside and outside the light cylinder. For $a/M = 0.9$, the light cylinder is at $R \approx 6r_g - 10r_g$. For the fiducial field line that threads the black hole (as given by equation (18)), the outer value of the cylindrical radius is $R \approx 120r_g$. Thus such a field line is far beyond the light cylinder. Field lines that thread the outer disk have not yet passed through their light cylinder, so we focus on the stability of the solution close to the black hole.

Once the solution became stationary by $t \sim 10^3 t_g$, random perturbations with an amplitude of 10% were added. The Poynting-jet from the black hole and the electromagnetic wind from the disk were found to be stable to these

perturbations within and far beyond the light cylinder where the toroidal field dominated. Thus, we can state that the axisymmetric pinch mode does not grow, at least in an Eulerian sense (though it may still grow in a Lagrangian sense moving out with the fluid and may manifest itself at large radii).

4.4 Dependence on Black Hole Spin

Now we study the dependence of the power on the black hole spin for GRMHD-motivated GRFFE models. In the GRMHD simulations, the value of Ω_F/Ω_H in the disk depends strongly on whether the spin is larger or smaller than $a/M \sim 0.4$, thus a mapping to a force-free model is not straight-forward because such force-free models choose an approximately fixed value of Ω_F/Ω_H for the entire magnetosphere above the equatorial plane. As described in McKinney & Narayan (2006), GRMHD models with black hole spins $a/M \gtrsim 0.4$ tend to have $\Omega_F/\Omega_H \sim 1/2$ on the horizon, and so using $\Omega_F/\Omega_H = 0.32$ in the GRFFE modeling should lead to a solution close to the GRMHD solution. However, for $a/M \lesssim 0.4$, the GRMHD solution within the disk is found to follow $\Omega_F/\Omega_H \sim 1$ because the disk dominates the field all the way through the horizon. Since the power from the black hole is $P \propto \Omega_F(\Omega_F - \Omega_H)(B^r)^2$, then $P \sim 0$ for $a/M \lesssim 0.4$.

We already know that the magnetosphere is free from unwanted discontinuities only if one chooses $\Omega_F/\Omega_H \sim 0.32$ on the horizon at the equator. One problem with modelling $a/M \lesssim 0.4$ black holes is that choosing the value of $\Omega_F/\Omega_H \sim 1$ would lead to discontinuities in the magnetosphere. Even if one allowed discontinuities, the more important problem is that the field lines passing through the horizon above the equator would still settle on having $\Omega_F/\Omega_H = 0.32$. Hence, while the power through the disk would vanish exactly at the equator, it would not vanish just off the equator. A comparable GRMHD simulation with a *thick* disk would have $P \sim 0$ over the *entire* part of the horizon occupied by the infalling disk material. In such models, as the disk thickness increases, the power (per unit $(B^r)^2$) drops because the disk takes over the magnetosphere. Thus, the disk thickness plays an important role in setting the total power output for $a/M \lesssim 0.4$.

Despite these complications, in the following we employ the *same model* of Ω_F/Ω_H in the disk for all black hole spins, but we primarily focus on the models with $a/M \gtrsim 0.5$ where the results are most representative of the GRMHD models for any disk thickness. We use equation (3) to model the disk rotation and equation (2) to soften the vector potential in the transition region.

Table 1 shows the electromagnetic power output, Lorentz factor, and half-opening angle for different black hole spins and at different radii. The power could be arbitrarily normalized, but we use two specific normalizations that are convenient for comparisons with the results from GRMHD models. In the upper section of the table, the power has been normalized by $(B^r)^2$ on the horizon at the poles of the *initial* $a/M = M = 0$ model with $\nu = 3/4$. Since the field strength at large radius is not significantly changed by the slow disk rotation or the rotation of the black hole, this is equivalent to a normalization by the *disk field strength at large radii*. If the accretion rate and field strength at large

radii can be established for a GRMHD model, then this is a good normalization to use for comparison with the GRFFE model. The lower section of the table has the power normalized by $(B^r)^2$ on the horizon at the poles of the *final* stationary model. This removes the changes in the field strength near the black hole due to the spin of the black hole. If the accretion rate at small radii is in force-balance with the field near the black hole, then this is a good normalization. However, the field strength near the horizon is a strong function of black hole spin (McKinney 2005a) and a mild function of the mass accretion rate, so this normalization should be considered carefully when comparing results for different black hole spins.

Regardless of the normalization, one interesting conclusion, from the table values for $P[r_+]$ to $P[r = 10^3 r_g]$, is that even at high black hole spins the disk provides no less than $\approx 1/4$ of the total power output.

The Lorentz factor and θ_j are independent of the normalization of course. The power shifts to small angles due to the emergence of the black hole component above $a/M \sim 0.5$, although this black hole component is always present. For the $a/M = 0.9$ model, the field line that connects to the black hole at the equator eventually reaches $\theta_j \approx 10^\circ$ at $r = 10^3 r_g$. The peak in the angular power density is set by the black hole power output for $a/M \gtrsim 0.9$ and is otherwise set by the disk power output.

If a disk were present with a sharply defined height to radius ratio of $H/R \approx 0.3$, as in the GRMHD numerical models, and the matter did not modify the poloidal field direction (which is a good approximation; see McKinney & Narayan 2006), then the field line would go from $\theta \approx 72^\circ$ on the horizon to $\theta_j \approx 10^\circ$ at $r = 10^3 r_g$. In the presence of both an accretion disk and corona, as in the GRMHD numerical models, with a combined scale-height to radius ratio of $H/R \approx 0.6$, then $\theta_j \approx 7^\circ$ at $r = 10^3 r_g$. Finally, if we extend the calculation to $r = 5 \times 10^3 r_g$ and again consider a disk+corona region blocking part of the power of the jet, then $\theta_j \approx 5^\circ$ there. This is the same jet collimation found for the core of the jet in time-dependent GRMHD numerical models (McKinney 2006c). In those simulations the jet had an extended low-energy wing out to $\theta_j \approx 27^\circ$, which could be due to the effects of matter or due to a lack of transfield pressure support at large radii. Overall the opening angle of the jet and the power output measured in the GRMHD numerical models and the $\nu = 3/4$ force-free models are in excellent agreement. A monopolar, paraboloidal, or cylindrical force-free model would not agree this well.

Figures 13 and 14 show the initial and final configurations of the field lines for the $a/M = 0.1$ and $a/M = 0.9375$ models, respectively. We see that the Keplerian rotation of the disk leads to some collimation of the disk field lines. On the other hand, the spin of the black hole leads to modest *decollimation* of the field lines near the poles.

4.5 Dependence on the Transition Model

Different models of the transition region were studied and Table 2 gives the same information as Table 1 for these different models.

The first model, called ‘‘TModel 1,’’ has been already discussed in §§ 4.3 and 4.4. It uses equation (3) for Ω_F with

Black Hole Spin Study							
a	P [r_+]	P [r_{ISCO}]	P [$10r_g$]	P [10^3r_g]	Γ [10^3r_g]	θ_j [10^3r_g] [Peak Power]	θ_j [5×10^3r_g] [$H/R = 0.6$]
Normalized by Disk Field Strength							
0.1	0.02415	0.5734	1.795	3.125	7	25°	4°
0.2	0.1122	1.283	2.694	3.995	8	25°	4°
0.5	0.7368	1.258	3.109	4.41	8	15°–26°	4°
0.8	1.893	2.632	5.721	6.92	10	15°–26°	4°
0.9	2.097	2.744	6.662	7.846	15	12°–26°	5°
0.9375	2.016	2.552	6.889	8.187	20	12°–26°	5°
Normalized by Black Hole Field Strength							
0.1	0.01562	0.3709	1.161	2.022	7	25°	4°
0.2	0.05428	0.6207	1.304	1.933	8	25°	4°
0.5	0.3417	0.5835	1.442	2.045	8	15°–26°	4°
0.8	0.5478	0.7618	1.656	2.003	10	15°–26°	4°
0.9	0.4715	0.6168	1.498	1.764	15	12°–26°	5°
0.9375	0.3905	0.4942	1.334	1.586	20	12°–26°	5°

Table 1. Electromagnetic Power, Lorentz factor, and half-opening angle of jet for different black hole spins and at a few radii for each model. The second to last column shows θ_j at the location of the peak in the angular power, which includes a significant power from disk at low black hole spins. The last column shows θ_j at a large radius for the field line that starts at $\theta_j = 57^\circ$ on the horizon, which begins the force-free region in GRMHD numerical models that have an accretion disk up to $H/R \approx 0.3$ and a corona up to $H/R \approx 0.6$.

Transition Model Study							
Model Type	P [r_+]	P [r_{ISCO}]	P [$10r_g$]	P [10^3r_g]	Γ [10^3r_g]	θ_j [10^3r_g] [Peak Power]	θ_j [5×10^3r_g] [$H/R = 0.6$]
Normalized by Disk Field Strength							
TModel 1	2.097	2.744	6.662	7.846	15	12°–26°	5°
TModel 2	1.672	1.938	3.983	4.65	15	15°–26°	5°
TModel 3	10.64	11.47	20.82	21.84	15	12°–26°	5°
Normalized by Black Hole Field Strength							
TModel 1	0.4715	0.6168	1.498	1.764	15	12°–26°	5°
TModel 2	0.4998	0.5794	1.191	1.39	15	15°–26°	5°
TModel 3	0.5063	0.5456	0.9906	1.039	15	12°–26°	5°

Table 2. Different models of the transition region are studied for a fixed black hole spin of $a/M = 0.9$. Otherwise similar to Table 1.

$\Omega_{\text{DBH}}/\Omega_H = 0.32$ and $r_{\text{trans}\Omega} = 2r_+$, and equation (2) for the vector potential with $r_{\text{transB}} = 2r_+$.

TModel 2

The second model, called “TModel 2,” uses equation (4) for Ω_F with $\Omega_{\text{DBH}}/\Omega_H = 0.32$, $r_{\text{trans}\Omega} = 3r_+$, and $r_0 = 2r_+$, and equation (2) with $r_{\text{transB}} = 2r_+$. This model can be used to study any a/M and has a smooth transition from a Keplerian Ω_F at large radii to a fixed Ω_F near the black hole. TModel 2 leads to qualitatively and quantitatively similar results as TModel 1.

TModel 3

The final model, called “TModel 3,” uses equation (3) for Ω_F with $\Omega_{\text{DBH}}/\Omega_H = 0.59$ and $r_{\text{trans}\Omega} = 2r_+$, and again equation (2) with $r_{\text{transB}} = r_+$. This last model is chosen to match most closely to the GRMHD transition regardless of whether additional discontinuities are created in the magnetosphere.

Most features of this model are qualitatively similar, such as the field lines as shown in Figure 14 and the power output distribution as shown in Figure 11. There are two new qualitative results, however. First, there are additional current sheets in the magnetosphere near the disk inside the ergosphere. This is due to Ω_F not matching between the disk and the black hole. These additional currents indicate

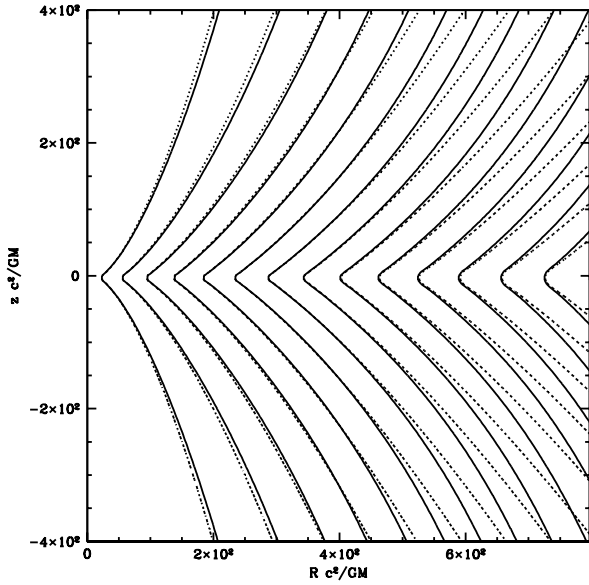


Figure 13. Field lines for the $a/M = 0.1$ GRFFE model with $\nu = 3/4$ at $t = 0$ (initial state, nonrotating solution, dotted lines) and $t = 1.2 \times 10^3 t_g$ (final converged rotating solution, solid lines). The field lines threading the black hole show mild decollimation, as in the paraboloidal case, and the field lines from the outer regions of the disk show some collimation.

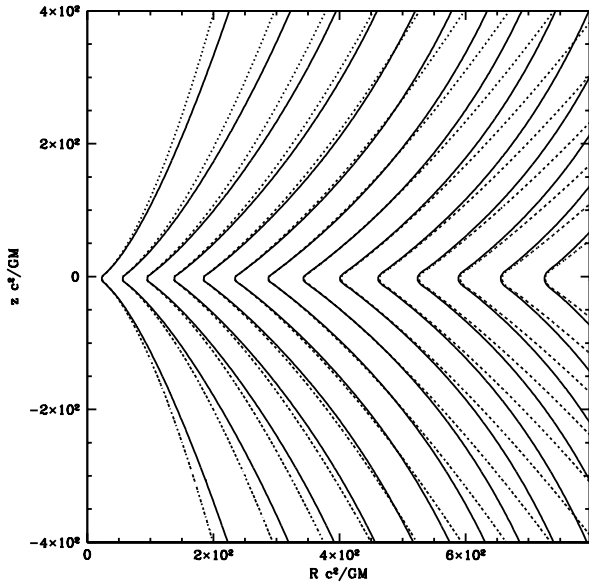


Figure 14. Similar to Figure 13, but for a rapidly spinning black hole with $a/M = 0.9375$. There is again mild decollimation of the field lines threading the black hole, and some collimation of field lines from the disk.

that no simple force-free solution can replace the matter-dominated disk. The second feature is that the field strength at the poles of the black hole is about $2.5\times$ more enhanced compared to the initial field strength. This field enhancement and the faster disk rotation leads to about $5\times$ more power output from the black hole and about $2\times$ more power from the disk if one normalizes the power by the disk field strength. This suggests that an accurate model of the transition region, only possible in full GRMHD, is important in obtaining a quantitative estimate for the power output.

Transition Model Summary

In summary, the accreting matter plays a significant role in setting up the transition region, and no trivial normalization of the force-free results can provide an unbiased estimate of the power output. In GRMHD models, the disk+corona absorbs much of the power that reaches large distances in the GRFFE models. Force-free models with a thick wedge to replace the disk+corona may better reproduce the power lost to the disk and corona.

However, we found that the qualitative behavior of the force-free Poynting-jet from the black hole does not depend on the details of the matter flow in the transition region between the disk and black hole. For a good estimate of the power output that would correspond to the power output found in GRMHD numerical models, one can truncate the power output in the GRFFE model to include that power only above the disk+corona scale height in the funnel that contains the Poynting-dominated jet. For the GRMHD models studied here, this angle away from the disk is $H/R \approx 0.6$. To convert the power output to physical units, one can use the dependence of the horizon magnetic field strength on the mass accretion rate and black hole spin found in GRMHD models (McKinney 2005a).

Quantitative estimates of the Lorentz factor and opening angle are insensitive to the details of the transition region. This is because with a $\nu = 3/4$ current distribution, the poloidal field direction does not significantly change for any changes in the disk or black hole angular frequency.

4.6 Comparison of GRMHD and GRFFE $a/M = 0.9375$ Models

Figure 15 shows the field geometry from a time-dependent GRMHD numerical model as shown in Figure 9 from McKinney & Narayan (2006), but now overlaid with the $a/M = 0.9375$ $\nu = 3/4$ GRFFE stationary solution for the poloidal field. The funnel region, along which the Poynting-dominated jet in the GRMHD model emerges, has a poloidal field reasonably consistent with the $\nu = 3/4$ current sheet solution.

Hoop-stresses can be discarded as important in helping to collimate the jet since the poloidal field geometry is *decollimated* by the action of the black hole spin, leading to even larger differences between the GRMHD and GRFFE poloidal fields near the poles compared to the differences found in McKinney & Narayan (2006) where we compared the polar field from the GRMHD solution and the nonrotating $\nu = 3/4$ force-free solution.

The field lines are more collimated in the GRMHD

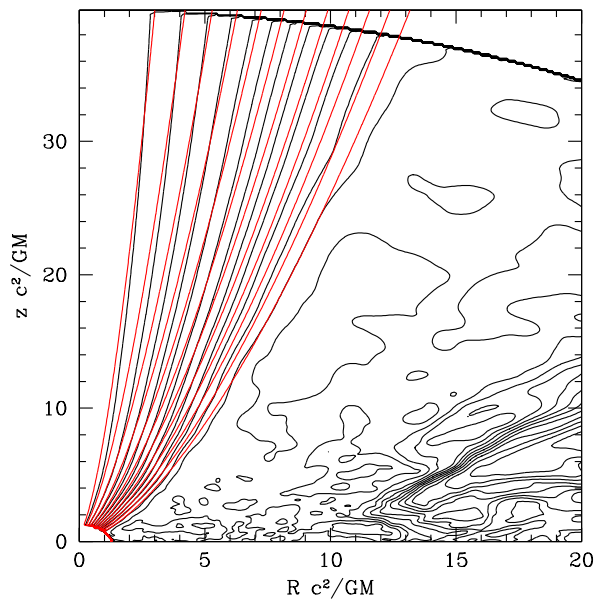


Figure 15. Overlay of the time-averaged poloidal field from the GRMHD numerical model of an accretion disk with a rapidly spinning black hole with $a/M = 0.9375$ (black) and the poloidal field from the numerical GRFFE model with $\nu = 3/4$ and the same value of a/M (red). Only the portion of the $\nu = 3/4$ GRFFE solution that overlaps the funnel region of the GRMHD model is shown. Note the excellent agreement between the two models in the overlap region. However, the agreement is no better than with the non-rotating $\nu = 3/4$ solution shown in Figure 9 of McKinney & Narayan (2006). Thus, while the choice $\nu = 3/4$ is key to obtain a good match in the poloidal field structure, the rotation of the disk and the black hole play a lesser role.

model than the GRFFE model for otherwise similar models. This is likely due to a small extra pressure support by the corona or coronal wind. Both polar axes show the same behavior, so this is not likely due to residual time-dependence in the GRMHD model. Despite this effect, the opening angle for most of the power output at large distances is similar for the GRMHD and GRFFE models. This means in the GRMHD models that the coronal wind provides some additional collimation, but the primary confinement of the Poynting-dominated jet is due to the corona. In the GRMHD models, the gas+magnetic pressure of the corona that contains no ordered field is found to be similar to the pressure provided by the force-free field in GRFFE models. This agreement between the pressures explains why the funnel field geometry is similar, but the process that sustains this balance is unknown and should be studied.

5 GRMHD DISK MODEL WITH INITIAL $\nu = 3/4$ GRFFE FIELD

In McKinney & Narayan (2006) we showed that the $\nu = 3/4$ power-law model represents well the currents measured in fully turbulent GRMHD numerical models. We have also in this paper shown that the magnetic field geometry and the power output in the Poynting-dominated funnel region near the poles of the black hole are properly modelled by the

$\nu = 3/4$ rotating force-free model. However, in the GRMHD models there are no ordered field lines that thread the disk or corona. What happens to these field lines?

In this section we study the process whereby the turbulence-driven convective and magnetic instabilities in the disk and corona destroy an ordered field. This process was discussed in McKinney & Gammie (2004); McKinney (2005a), where it was indicated that the final geometry of the field lines was nearly independent of the initial field geometry. The initial field geometries in those studies include a single field loop, many field loops with different poloidal directions, and a uniform net vertical field. In all cases, the final field geometry within the accretion disk, corona, and around the black hole was qualitatively similar (see also McKinney 2005a). Here we perform a similar study with the non-rotating $\nu = 3/4$ solution as the initial field geometry.

5.1 Numerical Setup

The GRMHD equations of motion are integrated numerically using a modified version of a numerical code called HARM (Gammie et al. 2003a), which uses a conservative, shock-capturing scheme. Compared to the original HARM, the inversion of conserved quantities to primitive variables is performed by using a new faster and more robust two-dimensional non-linear solver (Noble et al. 2006). A parabolic interpolation scheme (Colella 1984) is used rather than a linear interpolation scheme, and an optimal total variational diminishing (TVD) third order Runge-Kutta time stepping (Shu 1997) is used rather than the mid-point method. For the problems under consideration, the parabolic interpolation and third order time stepping method reduce the truncation error significantly, even in regions where $b^2/\rho_0 \gg 1$.

5.2 GRMHD Model with $\nu = 3/4$ Initial Field

The $\nu = 3/4$, $a/M = 0$ solution for the poloidal field is implanted in the same torus model of the accretion disk as studied in McKinney & Gammie (2004) and the GRMHD equations are integrated. As in the fiducial model of McKinney & Gammie (2004), the black hole has a spin of $a/M = 0.9375$, which is close to the equilibrium value of $a/M \sim 0.92$ (Gammie, Shapiro, & McKinney 2004).

As a reference point, Figure 16 shows the initial and final field geometry for the GRMHD model with $a/M = 0.9375$ with an initial field corresponding to a single field loop in the torus, as studied by McKinney & Gammie (2004) and others.

Figure 17 shows the initial and final field geometry for the GRMHD model with $a/M = 0.9375$ that uses the $\nu = 3/4$ force-free solution for the initial field geometry. A model initially with a net vertical field leads to qualitatively similar results. The GRMHD model with a single loop exhibits more turbulence and larger variations in the polar enclosed poloidal current, which at high/low levels saturates to red/black in the color figure.

The final poloidal field distribution at the poles follows the $\nu = 3/4$ force-free solution for both the models as shown in Figures 16 and 17. Other models, not shown, such as one with an initial net vertical field also agree with the $\nu = 3/4$

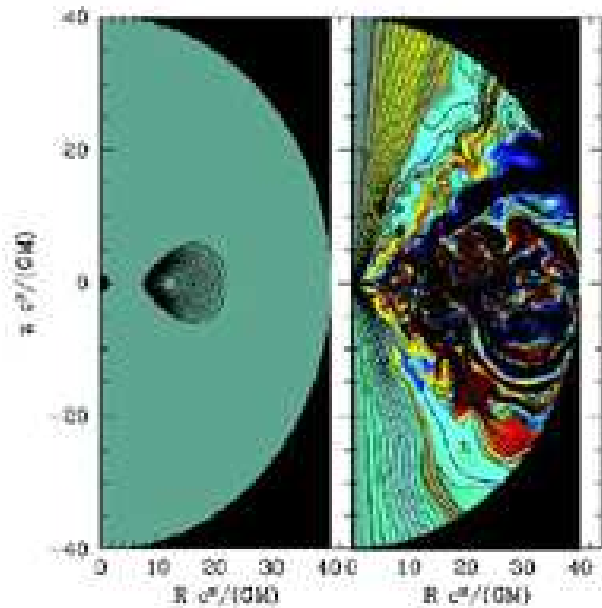


Figure 16. Initial (left panel) and final (right panel) poloidal magnetic field geometry (solid black lines) and toroidal field strength (B_ϕ , red positive, blue negative) for a GRMHD numerical model that was initiated with a gas torus containing a poloidal magnetic loop. The model has a rapidly spinning black hole with $a/M = 0.9375$. The panel on the right shows the standard result for a GRMHD numerical model of an accretion disk, in which the final system has a disk, corona and outflowing wind with disordered field, and a polar region (the Poynting-dominated jet) with highly ordered field.

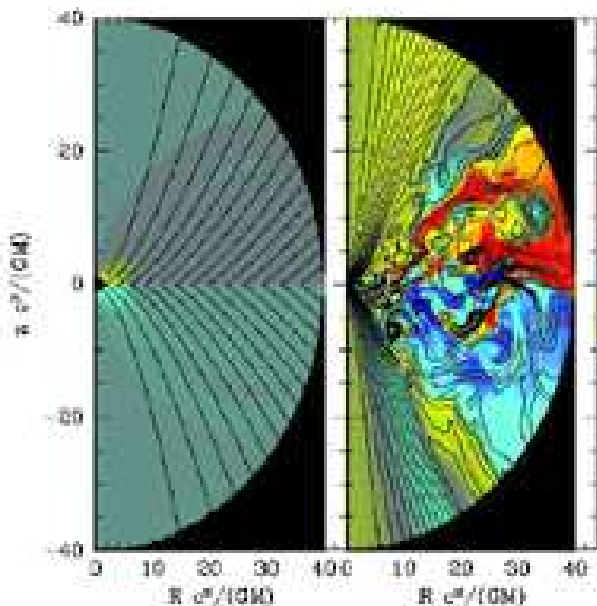


Figure 17. Similar to Figure 16 except that the initial magnetic field corresponds to the $\nu = 3/4$ force-free solution. Despite the very different initial conditions, the final states in the two models are similar.

force-free solution in the polar region. The value of Ω_F in the disk and transition region is also similar. This is despite the fact that the detailed structure of the magnetic geometry in the disk is different. For every model we have studied, the turbulence due to the magnetorotational instability efficiently redistributes the currents to the $\nu = 3/4$ power-law distribution.

For these models, the time evolution shows that the global magnetic field bifurcates into two regions. The funnel region forms as material with low angular momentum falls into the black hole and launches a jet, while many of the ordered fields threading the torus are tied to material that is gaining angular momentum and so is launched backwards along the disk surface.

As the bifurcation unfolds, the pressure support of the $\nu = 3/4$ field is lost in the region outside the funnel. As the disk accretes, some of the disk surface material resupplies that evacuated region to replace the pressure that was provided by the field. This process forms the corona and drives the disk wind.

A measurement of the gas+magnetic pressure in the coronal region shows that the evolved GRMHD model with the corona has a similar pressure as the initial force-free fields in that region. There is a small additional pressure driven by the flux of mass, and this explains why the GRMHD model is slightly more collimated than the force-free $\nu = 3/4$ model.

A similar quasi-stationary state of the accretion disk and field is found with various other initial field geometries (Hirose et al. 2004; McKinney 2005a). Only a contrived geometry with a purely toroidal field leads to significant deviations in the quasi-stationary state, and of course models with a purely toroidal field have no toroidal currents.

6 LIMITATIONS

The primary limitation of the present study is that the numerical models are axisymmetric. Therefore, while the GRFFE simulations show that the Poynting-dominated jet is stable to axisymmetric pinch perturbations, we cannot tell whether it is kink stable.

Another limitation is that in the GRFFE models the disk is assumed to be infinitely thin. This is in contrast to the GRMHD models where the disk is thick resulting in some power from the black hole being absorbed by the disk and corona. However, because the force-free region in the GRMHD simulations is sharply defined, a good estimate of the power can be obtained from the GRFFE models by limiting the integration of the angular power density to a cone around the poles that is the same angular size as that found in the GRMHD models. In this way, the Poynting-dominated jet power can be estimated for any disk thickness.

7 CONCLUSIONS

Motivated by the simple toroidal current distribution we found in GRMHD numerical models of turbulent accretion disks (McKinney & Narayan 2006), in this paper we have studied simple force-free (GRFFE) models of the black hole and disk magnetosphere. We idealized the GRMHD solution

for the accretion disk as an equatorial rotating conductor with boundary conditions defined by an equatorial toroidal current and field angular frequency.

To begin with, in § 3 we considered the paraboloidal problem of Blandford & Znajek (1977) in which the current is of the form $dI_\phi/dr \propto r^{-1}$. For a slowly rotating black hole and a non-rotating disk, we obtained excellent agreement between the numerical GRFFE solution and BZ's analytical solution; this is not surprising since the BZ solution was derived in this limit. We then considered a rapidly rotating black hole with a non-rotating disk and also a rotating hole with a Keplerian disk. In these cases, the GRFFE model deviates to some extent from the BZ solution, but the agreement between the two is still reasonably good. For all models, collimation was found to be primarily due to the poloidal field geometry determined by the toroidal current in the disk. Forces due to hoop-stresses nearly cancel centrifugal forces.

In paper I, we considered a self-similar force-free model of an equatorial current sheet with a toroidal current following $dI_\phi/dr \propto r^{-5/4}$ (the $\nu = 3/4$ model) (McKinney & Narayan 2006). In that paper we showed the structure of the field from the force-free solution agrees well with the poloidal field in the jet region of GRMHD numerical models. However, because the force-free model had no rotation, it had no toroidal field and we were unable to compare the toroidal structure or the Lorentz factor of GRMHD jets.

In § 4, we considered a similar force-free model with $dI_\phi/dr \propto r^{-5/4}$ in the equatorial plane, but with an arbitrarily rapidly rotating black hole and a Keplerian disk. One well-known subtlety of force-free models of the black hole and disk is how to define quantities within the transition region between the black hole and accretion disk (Blandford & Znajek 1977). We experimented with two different models, motivated by GRMHD simulations, for the field angular velocity in the transition region.

The agreement between these improved $\nu = 3/4$ GRFFE models and the jet/funnel region of the GRMHD models is excellent. We found that the poloidal structure of the field in the rotating GRFFE model is nearly the same as in the non-rotating model considered in McKinney & Narayan (2006), and like the latter agrees well with the poloidal structure of the field in the GRMHD jet. Within the jet driven by the black hole, forces due to hoop-stresses nearly cancel centrifugal forces, suggesting that self-collimation is not important. The toroidal field structure in the rotating GRFFE model agrees very well with the toroidal structure of the GRMHD jet, as do the power output in the jet and the Lorentz factor of the jet. Thus, the rotating GRFFE model gives an accurate description of the acceleration, collimation, jet opening angle, field pitch angle, electromagnetic power, etc., of the relativistic jet seen in GRMHD simulations.

While there is excellent agreement in the jet regions of the two solutions, there are large differences between the force-free and GRMHD models in other regions. In the force-free model the primary agent responsible for collimating the jet is the poloidal field threading the disk. These field lines lie external to the field lines in the jet (which thread the black hole), and it is the pressure of this external field that produces the collimation. In the GRMHD numerical model,

on the other hand, the region external to the jet is filled with a disorganized, magnetized corona and wind, and it is the pressure from this gas that causes the collimation. This suggests that the corona is required for the collimation of the Poynting-dominated jet in GRMHD simulations.

We also found that the GRFFE jet is stable to axisymmetric Eulerian perturbations. In the GRFFE model, the black hole jet is in force-balance with the force-free disk wind. In the GRMHD models of McKinney (2006c), we found that at large radii the jet is *unstable* to axisymmetric perturbations. This is consistent with the lack of coronal material (and so coronal pressure support that replaces the magnetized support in the force-free regime) at large radii. This suggests that astrophysical jets require support by a corona or disk wind in order to remain stable, but at large radii such support may be naturally unavailable and this may lead to toroidal-field-driven instabilities and dissipation in the jet as shown in McKinney (2006c).

The lack of an ordered field in the corona is related to the large difference between the GRFFE and GRMHD models with respect to the power output from the disk. In the force-free model, the disk field lines carry out electromagnetic power in the form of Poynting flux. In the GRMHD model, however, little electromagnetic power from the disk reaches large radii. Instead, most of the electromagnetic energy from the disk is dissipated in the matter and converted to other forms of energy in the plasma (McKinney & Narayan 2006).

In § 6, we described a numerical experiment in which we further explored the connection between the $\nu = 3/4$ ordered GRFFE solution and the magneto-rotationally unstable turbulent GRMHD model. An accretion disk was embedded with the $\nu = 3/4$ ordered field and followed using the GRMHD code. During the evolution of the system, the toroidal current in the disk retains its initial $\nu = 3/4$ behavior. However, the large-scale fields associated with the initial state are driven outwards by angular momentum transport and the pressure of those fields is replaced by coronal gas+magnetic pressure. This suggests that there is a continuous coupling between the currents in the disk and the coronal material. The corona and coronal wind are generated by reconnection processes and magnetic stresses in the disk. Even without an organized field the coronal wind is collimated, as suggested by Heinz & Begelman (2000); Li (2002). The gas+magnetic pressure in the corona is similar to the magnetic field pressure in the GRFFE model, and it is because of this that the jet regions are so similar in the two models. It remains unknown by what mechanism the pressure of the corona in GRMHD models drives the power-law $\nu = 3/4$ toroidal current that generates the corresponding magnetized jet.

ACKNOWLEDGMENTS

This research was supported by NASA-Astrophysics Theory Program grant NNG04GL38G and a Harvard CfA Institute for Theory and Computation fellowship. I thank Dmitri Uzdensky, Serguei Komissarov, and Vasily Beskin for useful comments and discussions.

APPENDIX A: ASYMPTOTIC FORM OF PITCH ANGLE AND LORENTZ FACTOR

In this appendix, we show how the Lorentz factor scales with radius for a given power-law distribution of currents in the disk. First, we remind the reader that the general relativistic language can be translated into an special relativistic language (3+1 splitting) by defining a space-time foliation. A convenient foliation is to choose to measure all quantities with respect to an observer with 4-velocity of a zero angular momentum observer (ZAMO) frame. This is given by $\eta_\mu = \{-\alpha, 0, 0, 0\}$, where $\alpha = 1/\sqrt{-g^{tt}}$. In this frame, the force-free equations take the same form as in Minkowski space-time.

In the ZAMO frame the drift velocity is written as

$$v^i = \frac{\epsilon^{ijk} E_j B_k}{B^2}, \quad (\text{A1})$$

where ϵ^{ijk} is the spatial permutation tensor. The Lorentz factor is given by

$$\Gamma = \frac{1}{\sqrt{1 - v^2}}, \quad (\text{A2})$$

as in special relativity. The electric field is given by

$$E^i = -\epsilon^{ijk} v_j B_k, \quad (\text{A3})$$

Given flux-freezing, axisymmetry, and stationarity, the fluid velocity or drift velocity is related to the magnetic field and field angular frequency via the relation

$$\frac{v_p}{B_p} = \frac{v_t - R\Omega_F}{B_t} \quad (\text{A4})$$

where these are orthonormal basis quantities where p stands for poloidal, t stands for toroidal, and R is cylindrical radius (Bekenstein & Oron 1978). For a review of the force-free equations see McKinney (2006a).

Now, consider the asymptotic regime where $r \rightarrow \infty$, and assume that the toroidal field dominates in this regime such that the mostly radial poloidal velocity approaches the speed of light. Then from equation (A3) one finds that

$$|E| \approx |E^\theta| \approx |B_t|. \quad (\text{A5})$$

From the drift velocity, one has that

$$v^2 = \frac{|\mathbf{E} \times \mathbf{B}|^2}{B^2(B_p^2 + B_t^2)^2} \approx \frac{E^2}{(B_p^2 + B_t^2)^2} \approx \frac{1}{(B_p/B_t)^2 + 1}, \quad (\text{A6})$$

and so the Lorentz factor can be written as

$$\Gamma \approx \frac{B_t}{B_p}. \quad (\text{A7})$$

Beyond the light cylinder, $v_t \ll R\Omega_F$ and assuming v_p approaches the speed of light, equation (A4) then gives that

$$\frac{B_t}{B_p} = -R\Omega_F. \quad (\text{A8})$$

Notice that this result is consistent with the numerical results of this paper, where we discuss the pitch angle such as given by equation (15).

The above implies that

$$\Gamma = R\Omega_F = \Omega_F r^{1-\alpha}, \quad (\text{A9})$$

for a field geometry that follows $\theta_j \propto r^{-\alpha}$. In general, for a solution with a current distribution with power-law index

ν , in the slow-rotation approximation, the minimal-torque solution (Michel 1969) gives an opening angle of approximately

$$\theta_j \propto r^{-\nu/2}, \quad (\text{A10})$$

and so

$$\Gamma \propto r^{1-\nu/2}. \quad (\text{A11})$$

For example, for the paraboloidal field geometry with $\nu = 1$, one has that $\theta_j \propto r^{-1/2}$, so that $\Gamma \propto r^{1/2}$. For $\nu = 3/4$ one has that $\theta_j \propto r^{-0.375}$ so that $\Gamma \propto r^{0.625}$. This basic scaling is fairly consistent with the results of this paper, where deviations are expected for a general black hole spin and disk rotation profile. See also Beskin (1997); Beskin et al. (1998); Beskin & Malyskhin (2000); Beskin & Nokhrina (2006); Narayan et al. (2006).

REFERENCES

- Appl, S., & Camenzind, M. 1992, A&A, 256, 354
 Appl, S., & Camenzind, M. 1993, A&A, 274, 699
 Balbus, S. A. & Hawley, J. F. 1991, ApJ, 376, 214
 Balbus, S. A., & Hawley, J. F. 1998, Reviews of Modern Physics, 70, 1
 Bekenstein, J. D., & Oron, E. 1978, Phys. Rev. D, 18, 1809
 Beskin, V. S., & Pariev, V. N. 1993, Phys. Uspekhi, 36, 529
 Beskin, V. S. 1997, Uspekhi Fizicheskikh Nauk, 40, 659
 Beskin, V. S., Kuznetsova, I. V., & Rafikov, R. R. 1998, MNRAS, 299, 341
 Beskin, V. S., & Malyskhin, L. M. 2000, Astronomy Letters, 26, 208
 Beskin, V. S., & Nokhrina, E. E. 2006, MNRAS, 367, 375
 Blandford, R. D. 1976, MNRAS, 176, 465
 Blandford, R. D. & Znajek, R. L. 1977, MNRAS, 179, 433
 Blandford, R. D., & Payne, D. G. 1982, MNRAS, 199, 883
 Bogovalov, S. V. 1997, A&A, 323, 634
 Bucciantini, N., Thompson, T. A., Arons, J., Quataert, E., & Del Zanna, L. 2006, MNRAS, 368, 1717
 Colella, P., & Woodward, P., 1984, JCP, 54, 174
 Contopoulos, J. 1994, ApJ, 432, 508
 Contopoulos, J., & Lovelace, R. V. E. 1994, ApJ, 429, 139
 Contopoulos, J. 1995a, ApJ, 446, 67
 Contopoulos, J. 1995b, ApJ, 450, 616
 DeVilliers, J., Hawley, J. F., & Krolik, J. H. 2003, ApJ, 599, 1238
 Fender, R., & Belloni, T. 2004, ARA&A, 42, 317
 Gammie, C.F. 1999, ApJ, 522, L57
 Gammie, C. F., McKinney, J. C., & Gábor Tóth 2003, ApJ, 589, 444
 Gammie, C. F., Shapiro, S. L., & McKinney, J. C. 2004, ApJ, 602, 312
 Ghosh, P. & Abramowicz, M. A. 1997, MNRAS, 292, 887
 Hawley, J. F., & Krolik, J. H. 2006, ApJ, 641, 103
 Heinz, S., & Begelman, M. C. 2000, ApJ, 535, 104
 Heyvaerts, J., & Norman, J. 1989, ApJ, 347, 1055
 Hirose, S., Krolik, J. H., De Villiers, J., & Hawley, J. F. 2004, ApJ, 606, 1083
 Komissarov, S. S. 2001, MNRAS, 326, L41
 Komissarov, S. S. 2002a, ArXiv Astrophysics e-prints, arXiv:astro-ph/0211141
 Komissarov, S. S. 2002b, MNRAS, 336, 759

- Komissarov, S. S. 2004, MNRAS, 350, 427
Komissarov, S. S. 2006, MNRAS, 367, 19
Li, Z.-Y., Chiueh, T., & Begelman, M. C. 1992, ApJ, 394, 459
Li, L. 2002, ApJ, 564, 108
Lovelace, R. V. E., Mehanian, C., Mobarrry, C. M., & Sulkanen, M. E. 1986, ApJS, 62, 1
Thorne, K. S., & MacDonald, D. 1982a, MNRAS, 198, 339
MacDonald, D. & Thorne, K. S. 1982b, MNRAS, 198, 345
MacDonald, D. A. 1984, MNRAS, 211, 313
McKinney, J. C., & Gammie, C. F. 2002, ApJ, 573, 728
McKinney, J. C. 2004, unpublished Ph.D. thesis, University of Illinois at Urbana-Champaign, <http://rainman.astro.uiuc.edu/~jon/research/thesis.pdf>
McKinney, J. C., & Gammie, C. F. 2004, ApJ, 611, 977
McKinney, J. C. 2005a, ApJ, 630, L5
McKinney, J. C. 2005b, astro-ph/0506368
McKinney, J. C. 2005c, astro-ph/0506369
McKinney, J. C. 2006a, MNRAS, 367, 1797
McKinney, J. C. 2006b, MNRAS, 368, L30
McKinney, J. C. 2006c, MNRAS, 368, 1561
McKinney, J. C. & Narayan, R. 2006, MNRAS, accepted (astro-ph/0607575)
Meliani, Z., Sauty, C., Vlahakis, N., Tsinganos, K., & Trussoni, E. 2006, A&A, 447, 797
Michel, F. C. 1969, ApJ, 158, 727
Michel, F. C. 1973, ApJ, 180, L133
Misner, C. W., Thorne, K. S., & Wheeler, J. A. 1973, Gravitation. San Francisco: W.H. Freeman and Co., 1973 (MWT)
Narayan, R., McKinney, J. C., & Farmer, A. J. 2006, MNRAS, accepted (astro-ph/0610817)
Nitta, S., Takahashi, M., & Tomimatsu, A. 1991, Phys. Rev. D, 44, 2295
Noble, S. C., Gammie, C. F., McKinney, J. C., & Del Zanna, L. 2006, ApJ, 641, 626
Okamoto, I. 1974, MNRAS, 167, 457
Okamoto, I. 1978, MNRAS, 185, 69
Shu, C.W., 1997, NASA/CR-97-206253, No.97-65
Spitkovsky, A. 2006, ApJ, 648, L51
Tomimatsu, A., Matsuoka, T., & Takahashi, M. 2001, Phys. Rev. D, 64, 123003
Uzdensky, D. A. 2004, ApJ, 603, 652
Uzdensky, D. A. 2005, ApJ, 620, 889